A deformation model of flexible, HAMR objects for accurate propagation under perturbations and the self-shadowing effects

Sittiporn Channumsin Matteo Ceriotti and Gianmarco Radice

Geo-Informatics and Space Technology Development Agency (GISTDA), Bangkok 10210, Thailand

School of Engineering, University of Glasgow, Glasgow G12 8QQ, United Kingdom

sittiporn@gistda.or.th matteo.ceriotti@glasgow.ac.uk Gianmarco.Radice@glasgow.ac.uk

ABSTRACT

A new type of space debris in near geosynchronous orbit (GEO) was recently discovered and later identified as exhibiting unique characteristics associated with high area-to-mass ratio (HAMR) objects, such as high rotation rates and high reflection properties. Observations have shown that this debris type is very sensitive to environmental disturbances, particularly solar radiation pressure, due to the fact that its motion depends on the actual effective area, orientation of that effective area, reflection properties and the area-to-mass ratio of the object is not stable over time. Previous investigations have modelled this type of debris as rigid bodies (constant area-to-mass ratios) or discrete deformed body however these simplifications will lead to inaccurate long term orbital predictions. This paper proposes a simple yet reliable model of a thin, deformable membrane based on multibody dynamics. The membrane is modelled as a series of flat plates, connected through joints, representing the flexibility of the membrane itself. The mass of the membrane, albeit low, is taken into account through lump masses at the joints. The attitude and orbital motion of this flexible membrane model is then propagated near GEO to predict its orbital evolution under the perturbations of solar radiation pressure, Earth's gravity field (J2), third body gravitational fields (the Sun and Moon) and self-shadowing. These results are then compared to those obtained for two rigid body models (cannonball and flat rigid plate). In addition, Monte Carlo simulations of the flexible model by varying initial attitude and deformation angle (different shape) are investigated and compared with the two rigid models (cannonball and flat rigid plate) over a period of 100 days. The numerical results demonstrate that cannonball and rigid flat plate are not appropriate to capture the true dynamical evolution of these objects, at the cost of increased computational time.

Keywords: High area-to-mass ratio debris; Deformation model; Flexible model; Multilayer insulation; Self-shadowing, Monte Carlo

1. INTRODUCTION

In 2004, uncatalogued debris with high area-to-mass ratio (HAMR) in near geostationary orbits (GEO) were detected by Schildknecht. Analysis of the light curve of these objects shows that they display rapid rotation and their orbital evolutions are significantly perturbed in the GEO environment (Schildknecht et al., 2004, Schildknecht et al., 2008a, Schildknecht et al., 2008b, Früh and Schildknecht, 2011). Following detailed observations and laboratory-based analysis, it is thought that these objects could be multilayer insulation (MLI) pieces that delaminated from spacecraft due to aging, explosions or collisions (Dever et al., 1998, Sen et al., 2012, Murakami et al., 2008). MLI is used to cover all major outer surfaces of typical spacecraft as well as individual components to minimize heat transfer by separating the individual layers either by spatial separation or by insertion of low conductance spacer material. Multiple layers of thin, metalized substrate materials are then combined to from insulating blankets. The basic substrates are extremely thin layers material of PET®, Kapton® and Teflon®. These substrates, coated with a very thin layer of metal (aluminium, gold or silver on one or both sides of substrate) with thickness of the order of 1000 Å, are very lightweight, flexible and have low outgassing properties in a vacuum environment. Satellite buses may be covered by more than 20 layers while Sun shield for radio frequency antenna typically consist of less than five layers of MLI (Sheldahl, 2012).

The long term orbital evolution of HAMR objects under GEO perturbations has been studied by using a cannonball model that approximates the attitude motion and assumes the area-to-mass ratio (AMR) as constant. The motion of HAMR objects is however highly perturbed particularly due to direct solar radiation pressure and small changes in the effective AMR, which leads to significant changes in their orbital evolution. (Liou and Weaver, 2005, Valk et al., 2008a, Valk and Lemaître, 2008, Valk et al., 2008b, Rosengren and Scheeres, 2013). The real observations of this debris, however, indicated that the AMR values may change over time and hence the objects exhibit rapid attitude changes. This observation suggested that complex rotation, irregular shape and deformation of the actual object could lead to change AMR values (Früh and Schildknecht, 2012). The cannonball model is, therefore, not a good approximation for this debris type.

The coupling of attitude and orbital dynamics in near GEO for a short term propagation was investigated by Früh (Früh et al., 2013) with real MLI (PET® and Kapton®). The debris is there modelled as a flat rigid plate and assumed to have a constant area-to-mass ratio. The results show that the main tumbling rate is high due to SRP forces for both uniform and non-uniform reflection properties. The changes of the attitude motion lead to variations in both inclination and eccentricity. The Earth shadow effect and self-shadowing, which induce torques that lead to significant changes to the attitude and orbital elements in short and long-term evolution, are also considered (Früh et al., 2013, Hubaux and Lemaitre, 2013, Früh and Jah, 2014). Recently, Früh suggested that electrostatic charging may also affect the orbital dynamics (Früh et al., 2014). Another work (McMahon and Scheeres, 2013) studied the effects of solar radiation on different MLI configurations. The HAMR model can assume one of five different discrete shapes. The condition of the shape change depends on the objects's spin rate. The underlying idea behind this model is that when an object increases its tumbling rate, the material will tend towards a flatter geometry. The results of McMahon's investigations show that SRP torque strongly affects the fast attitude dynamics of this debris type. McMahon (McMahon and Scheeres, 2015) continued to study the alternative SRP model based on an Fourier series to improve SRP force model on an object. His investigation proofs that cannonball is not a good representation of the true SRP forces acting on the HAMR objects. The more realistic SRP force model allows to improve a precise orbit determination with realistic covariance bounds and sensor tracking.

In all the above studies (Früh et al., 2013, McMahon and Scheeres, 2013, Früh et al., 2014, Früh and Jah, 2014) the HAMR objects are assumed as rigid or discrete deformed bodies. This simplification is, however, inadequate to provide a more accurate prediction of both short term and long term orbital motion. The orbits of HAMR objects are highly sensitive and relatively small changes in the effective AMR can have a strong influence on their orbital evolution.

In this paper the MLI debris is modelled by means of multibody dynamics. Both attitude and orbital equations of motion are considered for motion propagation. Due to their deformations, HAMR objects may self-shade leading to change in the effective cross-sectional area. This work considers self-shadowing, adapting the algorithm in planar shadow projection (Williams, 1978) to address planar surfaces (Blinn, 1988). The result is, therefore, not only the prediction of the orbital evolution, but also the attitude and the deformation state of the membrane. The two substrates of MLI debris considered here are PET® and Kapton® (Sheldahl, 2012). The orbit and attitude motion are studied under perturbations due to J_2, solar radiation pressure and third body gravitation from the Sun and Moon in the GEO region, and compared with the orbital dynamics of two rigid models (cannonball and flat rigid plate) under the same environmental conditions. The approach is tested using a Monte Carlo simulation, varying the initial conditions (attitude dynamics and deformation state), and comparing the results of the propagation to conventional rigid body and cannonball models.

2. FLEXIBLE MULTIBODY MODEL

In principle, a flexible plate of MLI, which is a thin and lightweight reflective material, has infinite degrees of freedom (DOF). The Finite Element Method (FEM) analysis provides the high accuracy behaviour of a membrane leading to the high precision of solar radiation acting on the object but it is a difficult approach to implement within a numerical propagation due to enormous

computational costs. This paper aims to develop a model that allows reducing the degrees of freedom, to allow integration of the dynamical equations in a reasonable amount of computational time. The basic idea is that the solar radiation pressure depends on shape, reflection properties on the surface and attitude motion of an object. Therefore, the shape of the flexible model does not require to be described completely but it is sufficient to find an equivalent exposed area and the reflection properties. The actual SRP force on the body can then be computed by integrating the pressure on each surface element exposed to solar radiation (Kubo-oka and Sengoku, 1999, Mozurkewich, 2011, McMahon and Scheeres, 2013). These results are able to approximate the deformed model and provide a possible way, given a reasonable amount of computational power, to integrate orbital and attitude mechanics.

A thin and highly flexible MLI membrane is modelled with a multibody approach and the equations solved through Newtonian mechanics. The assumption is that the thin membrane in Fig 1 is capable of bending along each folding line and the deformation is described as a two-dimensional problem. The membrane is modelled as a series of lump masses, interconnected with rigid rods. The lump masses act as rotational joints for the plate and include rotational springs and dampers to simulate the bending stiffness of the membrane. The more lump masses, the more accurate the dynamics; however this comes at the expense of computational cost, and difficulty in determining the initial conditions accurately; even with accurate dynamics, the prediction of the orbit is invalid if the initial conditions are not exact. For this preliminary study, only three lump masses are considered (Fig 2(a)), connected through two rigid rods in order to simplify the model and reduce computational costs. The mass in the middle acts as a rotational hinge with spring

and damper. Essentially, this model concentrates the distributed mass of the MLI plate on lump masses, and its stiffness and damping properties on the central hinge. The plate is assumed infinitely rigid in the plane of the membrane itself. The deformed geometry of flexible model is defined the deformation angle (θ_d) as shown in Fig 2(b). The dimensions of flexible model are 1 meter in width and 1 meter in length and the length of both rigid rods ($l_1 = l_2 = l$) is 0.5 m, as in Fig 2.
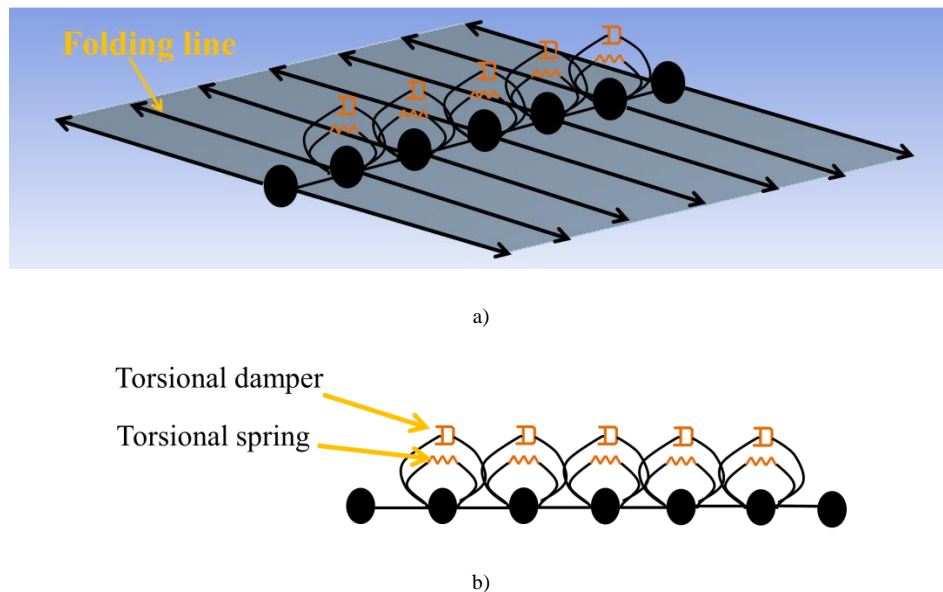

a)

b)

Fig 1 Comparing a flexible model with a thin membrane a) flat plate in 3D view b) side view.
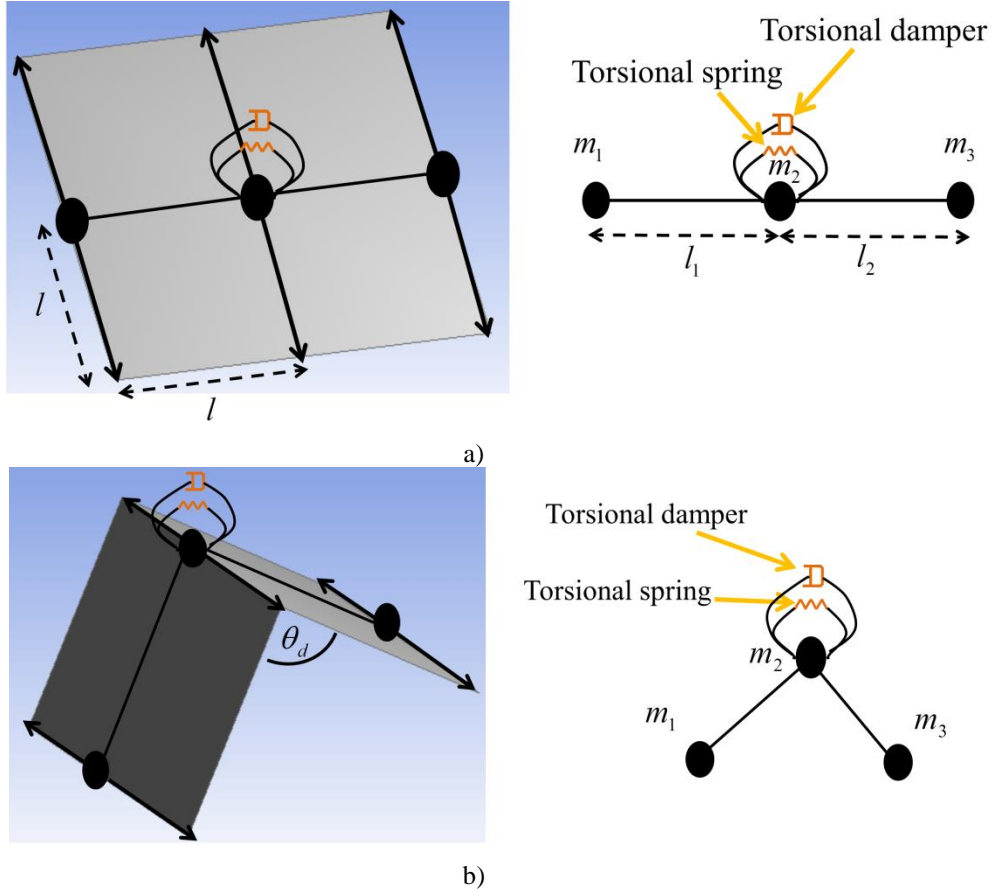
Fig 2 Simplified models as three lump masses installed with torsional damper and spring in 3D view and side view a) flat plate shape b) deformed shape.
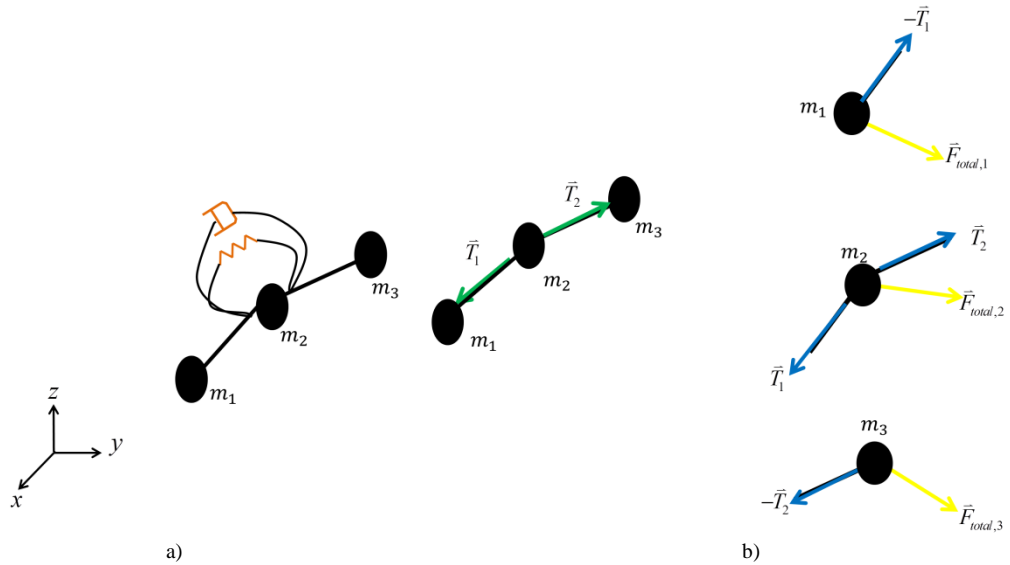

Fig 3 Flexible model a) The model in the inertial frame b) Free body diagram on each lump mass.

To analyse the forces acting on each mass in Fig 3, Newton's second law of motion leads to:

$$\vec{F}_{total,1} - \vec{T}_1 = m_1\ddot{\vec{x}}_1 \tag{1}$$

$$\vec{F}_{total,2} + \vec{T}_1 + \vec{T}_2 = m_2\ddot{\vec{x}}_2 \tag{2}$$

$$\vec{F}_{total,3} - \vec{T}_2 = m_3\ddot{\vec{x}}_3 \tag{3}$$

Where m_1 is i^{th} lump mass ($i = 1, 2$ and 3), $\vec{F}_{total,i}$ is total force vector acting on the ith lump mass ($\vec{F}_{total,i} = \vec{F}_{ext,i} + \vec{F}_{s,i} + \vec{F}_{d,i}$), $\vec{F}_{ext,i}$ is the external force vector from conservative and non-conservative perturbations (J2, SRP and the third-body from the Sun and the Moon), $\vec{T}_j$ is the tension force generated by the jth rod ($j = 1$ and 2), $\vec{F}_{s,i}$ is the rotational spring force vector of ith mass, $\vec{F}_{d,i}$ is the rotational damper force vector of ith mass, From these equations, we can calculate the total acceleration vector ($\ddot{\vec{x}}_i$) for each mass in an inertial frame:

$$\ddot{\vec{x}}_1 = (\vec{F}_{total,1} - \vec{T}_1) / m_1 \tag{4}$$

$$\ddot{\vec{x}}_2 = (\vec{F}_{total,2} + \vec{T}_1 + \vec{T}_2) / m_2 \tag{5}$$

$$\ddot{\vec{x}}_3 = (\vec{F}_{total,3} - \vec{T}_2) / m_3 \tag{6}$$

Then, we simplify the characteristic of a membrane (internal force: stress, strain and etc.) by representing rotational spring and damper for this model. Therefore, the rotational spring force is:

$$\vec{F}_{s,i} = k_s \theta_d / l \tag{7}$$

$$k_s = E_y I / l$$

Where k_s is rotational spring constant (bending stiffness of a membrane), E_y is Young modulus of material, I is the moment of inertia of the cross section area, l is the length of rod and the rotational damping force vector is:

$$\vec{F}_{d,i} = c_s \dot{\theta}_d / l \tag{8}$$

$$c_s = D_F \sqrt{M k_s}$$

Where c_s is the rotational damping constant, $\dot{\theta}_d$ is angular velocity of the deformation, D_F is dissipation factor of the material (Goodfellow, 2014), M is total mass of membrane.

To enforce that the distance between the masses shall be constant (as the membrane cannot stretch in its own plane, but only bend out of it), the constraint equations are:

$$(x_{j+1} - x_j)^2 + (y_{j+1} - y_j)^2 + (z_{j+1} - z_j)^2 = l_j^2 \tag{9}$$

Then the 2nd differential of Eq. (9) is expressed as:

$$2(\ddot{x}_j - \ddot{x}_{j+1})(x_j - x_{j+1}) + 2(\ddot{y}_j - \ddot{y}_{j+1})(y_j - y_{j+1}) + 2(\ddot{z}_j - \ddot{z}_{j+1})(z_j - z_{j+1}) + 2(\dot{x}_j - \dot{x}_{j+1})^2 + 2(\dot{y}_j - \dot{y}_{j+1})^2 + 2(\dot{z}_j - \dot{z}_{j+1})^2 = 0 \tag{10}$$

Finally, in order to complete the dynamic equations, we substitute the acceleration vectors of each mass in Eq. (10) in both rigid rods (j=1 and 2) to find the tension of both rods ($\vec{T}_1$ and $\vec{T}_2$) and write in matrix form:

$$\begin{bmatrix} C_1 & C_2 \\ C_3 & C_4 \end{bmatrix} \begin{bmatrix} \vec{T}_1 \\ \vec{T}_2 \end{bmatrix} = \begin{bmatrix} A_1 \\ A_2 \end{bmatrix} \tag{11}$$

Where

$$C_1 = (\vec{x}_1 - \vec{x}_2)(\frac{1}{m_1} + \frac{1}{m_2})$$

$$C_2 = -\frac{(\vec{x}_1 - \vec{x}_2)}{m_2}$$

$$C_3 = -\frac{(\vec{x}_2 - \vec{x}_3)}{m_2}$$

$$C_4 = (\bar{x}_2 - \bar{x}_3)(\frac{1}{m_2} + \frac{1}{m_3})$$

$$A_1 = -(\dot{x}_1 - \dot{x}_2)^2 - (\dot{y}_1 - \dot{y}_2)^2 - (\dot{z}_1 - \dot{z}_2)^2 - \vec{F}_{total,1}\frac{(\bar{x}_1 - \bar{x}_2)}{m_1} + \vec{F}_{total,2}\frac{(\bar{x}_1 - \bar{x}_2)}{m_2}$$

$$A_2 = -(\dot{x}_2 - \dot{x}_3)^2 - (\dot{y}_2 - \dot{y}_3)^2 - (\dot{z}_2 - \dot{z}_3)^2 - \vec{F}_{total,2}\frac{(\bar{x}_2 - \bar{x}_3)}{m_2} + \vec{F}_{total,3}\frac{(\bar{x}_2 - \bar{x}_3)}{m_3}$$

Then, we can find $\vec{T}_1$ and $\vec{T}_2$ by left-multiplying by the inverse matrix [C].

$$\begin{bmatrix} \vec{T}_1 \\ \vec{T}_2 \end{bmatrix} = \begin{bmatrix} C_1 & C_2 \\ C_3 & C_4 \end{bmatrix}^{-1} \begin{bmatrix} A_1 \\ A_2 \end{bmatrix} \tag{12}$$

Finally, the accelerations of each lump mass can be found through Eq.(4) – (6) to study the orbital evolution.

2.1 External torques of flexible model

The different external forces on the lump mass induce torques acting on the flexible model that causes the deformation. In this paper, we consider the gravity gradient torque and solar radiation torques as shown in Fig 4.
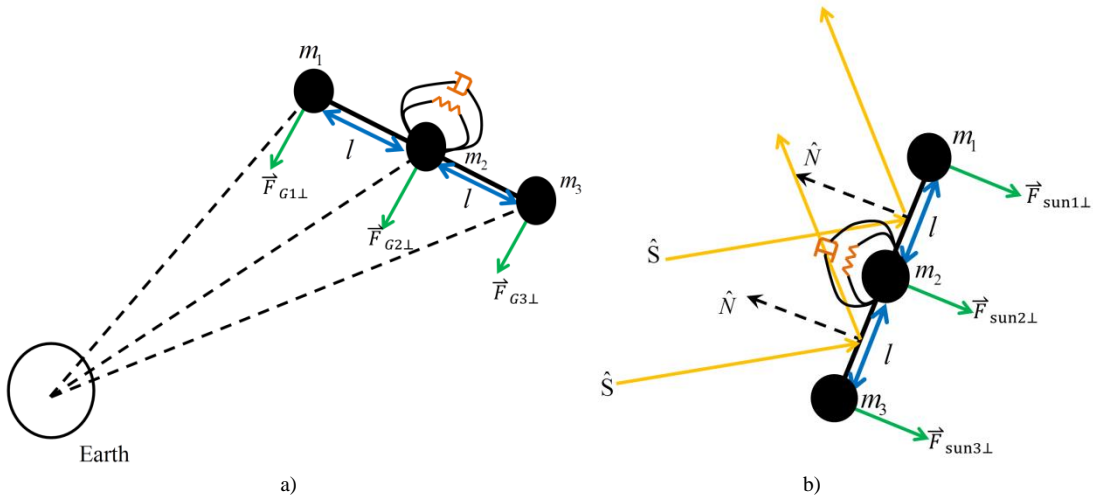

Fig 4 External torque acting on the flexible model a) Gravity gradient torque b) Solar radiation torque.

2.1.1 Gravity gradient torque

The gravitational forces acting on each lump mass are illustrated in Fig 4(a). The difference in the normal component of the gravitational forces results in a gravitational torque at each node, given by:

$$\vec{M}_{G,j} = (\vec{F}_{G(j)\perp} - \vec{F}_{G(j+1)\perp})l \tag{13}$$

Where $\vec{M}_{G,j}$ is the gravitational torque of jth rod (j =1 and 2) and $\vec{F}_{G(j)\perp}$ is a perpendicular gravitational force of the jth lump mass on j^{th} rod, $\vec{F}_{G(j+1)\perp}$ is a perpendicular gravitational force of the $j+1^{th}$ lump mass on j^{th} rod.

2.1.2 Solar radiation torque

We consider the solar rays acting on each rod in Fig 4(b). This SRP force on a rod will pass through on the two lump masses connected with that rod. The SRP torque on each rod is generated when the perpendicular SRP forces on the two lump masses on the same rod are different that is given as:

$$\vec{M}_{sun,j} = (\vec{F}_{sun(j)\perp} - \vec{F}_{sun(j+1)\perp})l \tag{14}$$

Where $\bar{M}_{sun,j}$ is the solar radiation torque of jth rod, $\bar{F}_{sun(j)\perp}$ is a perpendicular SRP force of the jth lump mass on j^{th} rod and $\bar{F}_{sun(j+1)\perp}$ is a perpendicular SRP force of the $j+1^{th}$ lump mass on j^{th} rod.

2.2 Numerical Model

The first test is to analyse the deformations arising from the presence of a rotational spring and damper and then the model will be forced to simulate a movement and rotation of the flexible model. In this section, each lump mass is defined as 1 kg and the characteristic parameters for the rotational spring and damper are assumed to be k_s = 0.01 N·m/rad and c_s = 0.05 N·m·s/rad respectively. These values are unrealistic for MLI membranes, and are only used for the purpose of testing the model and analyse its response.

2.2.1 Rotational spring and damper test

In order to test the rotational spring and damper of the model, an initial shape is required to set a non-flat geometry as a triangular shape in Fig 5(a) to activate both functions. Firstly, we consider the case of spring only, without damping. The continuous oscillation of the model in Fig 5(b) is forced by the rotational spring. If we consider both spring and damper in Fig 5(c), then it can be seen that the damper reduces the amplitude of the oscillation until motion stops completely.

a)

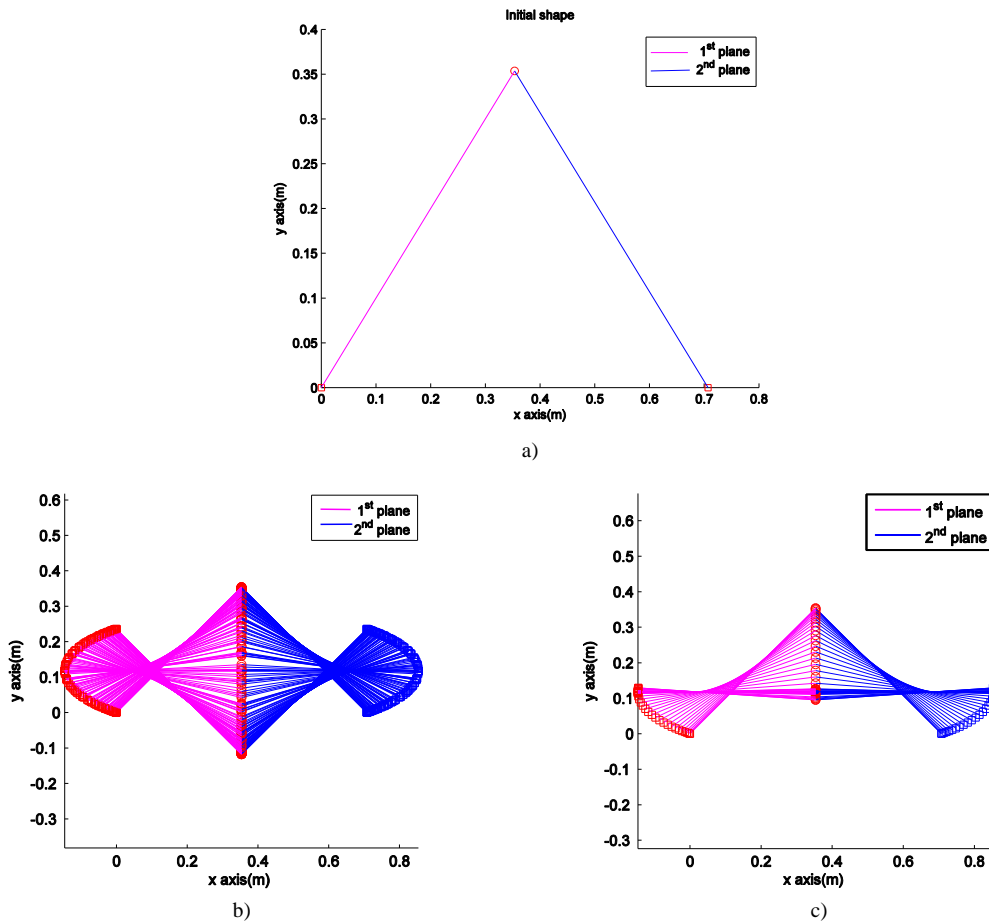b)   c)

Fig 5 Simulation of flexible model without external force a) initial geometry before simulation (triangular shape) b) time-lapse of the deformation when only the spring is considered, leading to unlimited oscillations c) time-lapse of the deformation when both spring and damper are considered. The damper quickly dampens the oscillation (7 lines/1 second).

2.1.2 Displacement and rotation test

This model is tested in 4 different cases. In the first and second test (Fig 6 and Fig 7), a continuous force of 1 N in the y direction and 1 N in both x and y directions is applied on all lump masses for 10 seconds. The flexible model will not show any deformation due to the fact that the same force is acting on each lump mass. The body moves in the direction of the force with increasing velocity. In the third case in Fig 8(a) a force of 1 N is applied for 1 second, only on the central mass in the z direction. The results show that the two plates move up and down in the z direction due to the presence of the spring in Fig 8. In the last test in Fig 9, a force of 1 N is applied for 1 second along both x and z directions on the first lump mass. The results show that in this case the model rotates and translates following the direction of the applied force in Fig 9(b). The results show that the f model is capable of describing 6 DOFs (3 linear and 3 angular motions) when different force vectors are acting on the lump masses.

a)   b)
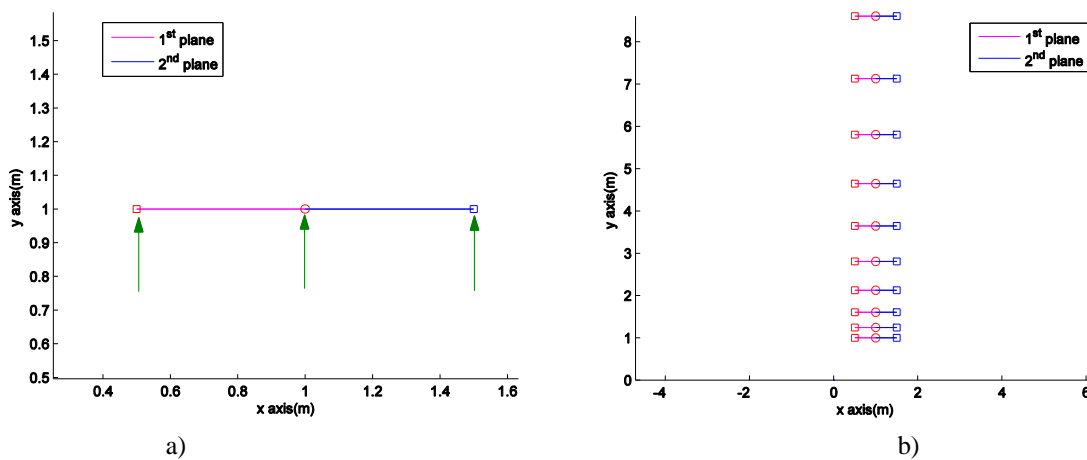
Fig 6 Simulation of flexible model for 10 seconds with external force, 1 N (arrow) in y direction on each lump mass continuously a) initial position in 2D view b) direction of movement in 2D view (1 line/0.6 seconds).

a)   b)
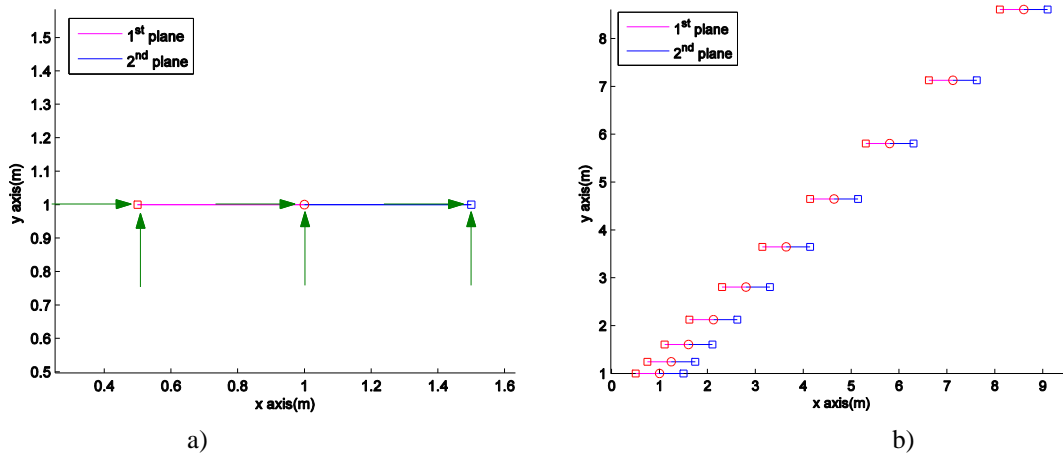
Fig 7 Simulation of flexible model in 10 seconds with external force 1 N (arrow) in x and y directions on each lump mass continuously a) initial position in 2D view b) direction of movement in 2D view (1 line/0.6 seconds).
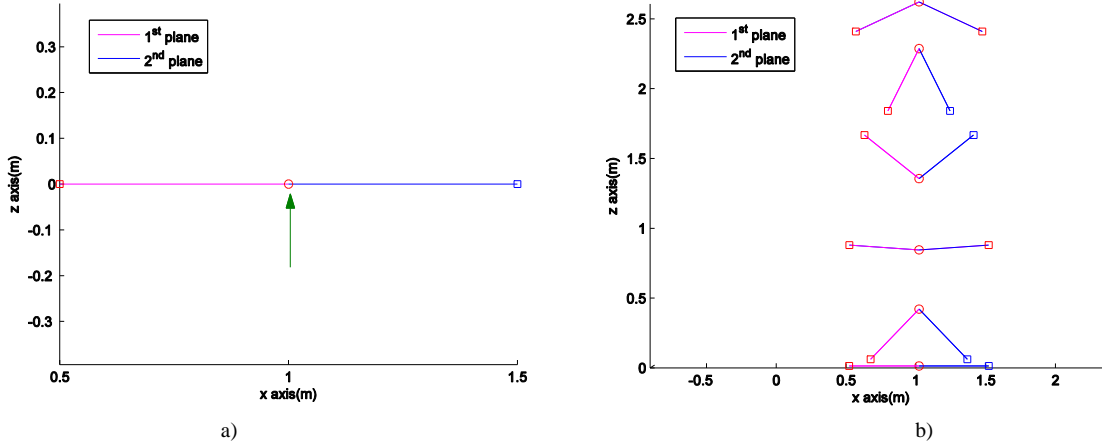
Fig 8 Simulation of flexible model for 8 seconds with external force 1 N for one second (arrow), in z directions on each lump mass a) initial position in 3D view b) direction of movement in 3D view (1 line/1.33 seconds).
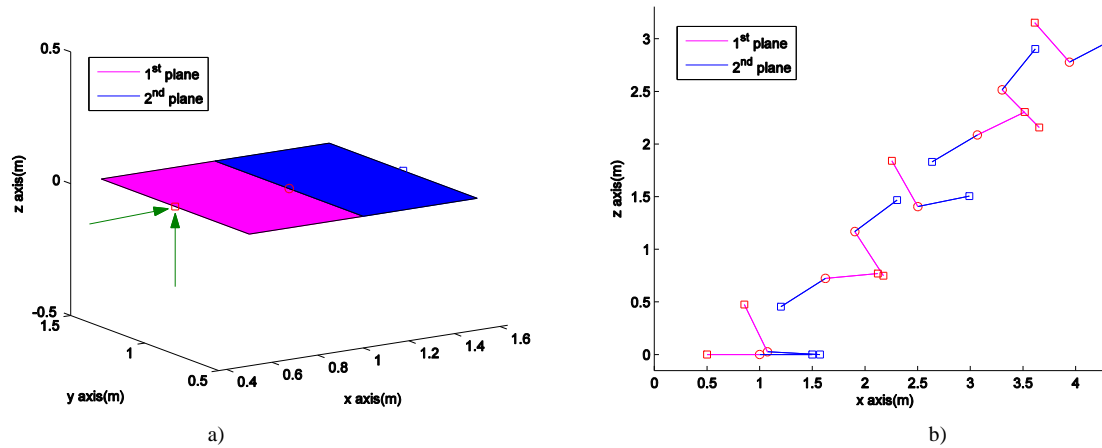

Fig 9 Simulation of flexible model for 8 seconds with external force 1 N for one second (arrow) in x and z directions on each lump mass a) initial position in 3D view b) direction of movement in 3D view (1 line/1.33 seconds).

3. ORBITAL AND ATTITUDE DYNAMICS

In this paper, the objects are assumed to be located in near geosynchronous Earth orbit (GEO). The main perturbations affecting their orbital and attitude dynamics are caused by Earth oblateness (J_2), third body gravitational fields (Sun and Moon) and solar radiation pressure.

3.1 Orbital Dynamics

The set of orbital elements, described by Gaussian variation of parameters (VOP), are here chosen to study the orbital evolution. This method has a singularity problem when the eccentricity and orbital inclination are equal to 1 and 90 degrees respectively. To avoid this singularity, the modified equinoctial orbital elements (MEE) (Walker et al., 1985) were introduced. The set of MEE equations are defined in terms of the equinoctial orbital elements (EQU) as follows:

$$p = a(1 - e^2)$$ (15)

$$f = e\cos(\omega + \Omega)$$

$$g = e\sin(\omega + \Omega)$$

$$h = \tan(i/2)\cos\Omega$$

$$k = \tan(i/2)\sin\Omega$$

$$L = \Omega + \omega + v$$

Where a is the semi-major axis, e is the eccentricity, i is the inclination, ω is the argument of perigee, Ω is the right ascension of ascending node, v is the true anomaly, p is semilatus rectum and L is true longitude. The variation of the modified equinoctial elements is expressed in:

$$\dot{p} = \frac{2p}{w}\sqrt{\frac{p}{\mu}}\Delta_t \tag{16}$$

$$\dot{f} = \sqrt{\frac{p}{\mu}}\left(\Delta_r \sin L + \left((w+1)\cos L + f\right)\frac{\Delta_t}{w} - (h\sin L - k\cos L)\frac{g\Delta_n}{w}\right)$$

$$\dot{g} = \sqrt{\frac{p}{\mu}}\left(-\Delta_r \cos L + \left((w+1)\cos L + g\right)\frac{\Delta_t}{w} - (h\sin L - k\cos L)\frac{f\Delta_n}{w}\right)$$

$$\dot{h} = \sqrt{\frac{p}{\mu}}\frac{s^2}{2w}\cos L\Delta_n$$

$$\dot{k} = \sqrt{\frac{p}{\mu}}\frac{s^2}{2w}\sin L\Delta_n$$

$$\dot{L}_i = \sqrt{\mu p}\left(\frac{w}{p}\right)^2 + \frac{1}{w}\sqrt{\frac{p}{\mu}}(h\sin L - k\cos L)\Delta_n$$

Where μ is the Earth's gravitational parameter (3.986005×10^{14} m^3/s^2), $\Delta_r, \Delta_t, \Delta_n$ are the non-two-body perturbations in the radial ($\vec{r}$), tangential ($\vec{t}$) and normal ($\vec{n}$) directions respectively, $s = \sqrt{1+h^2+k^2}$ and $w = 1 + f\cos L + g\sin L$.

We consider J$_2$, third body perturbations from the Sun and Moon and SRP perturbations. Therefore, the total perturbing acceleration is expressed as:

$$\bar{\Delta} = \bar{a}_{J_2} + \bar{a}_{sun} + \bar{a}_{moon} + \bar{a}_{SRP} \tag{17}$$

Planetary oblateness is considered through the J$_2$ harmonic (Seeber, 1993). The gravitational potential of the Earth due to the oblateness effect is expressed as:

$$R_{2,0} = -\frac{1}{2}\mu J_2 \frac{R_\oplus^2}{\bar{x}^3}(3\sin^2\varphi - 1) \tag{18}$$

Where J$_2$ is the 2th zonal harmonic coefficient (1.0826269×10^{-3}), $R_\oplus$ is the radius of the Earth (6,378.137 km), $\bar{x}$ is the geocentric position of the debris and φ is the geocentric latitude of the object in the Earth fixed frame. Therefore, the 2nd differential of Eq.(18) is J$_2$ acceleration ($\bar{a}_{J_2}$) along each component of inertial reference frame as:

$$a_{J_2,I} = \frac{\partial R_2}{\partial x_I} = -\frac{3\mu J_2 R_\oplus^2 x_I}{2x^5}\left(1 - \frac{5x_K^2}{x^2}\right) \tag{19}$$

$$a_{J_2,J} = \frac{\partial R_2}{\partial x_J} = -\frac{3\mu J_2 R_\oplus^2 x_J}{2x^5}\left(1 - \frac{5x_K^2}{x^2}\right)$$

$$a_{J_2,K} = \frac{\partial R_2}{\partial x_K} = -\frac{3\mu J_2 R_\oplus^2 x_K}{2x^5}\left(3 - \frac{5x_K^2}{x^2}\right)$$

The third body gravity forces due to the Sun and Moon (Vallado, 2007) with respect to the Earth's centre of mass are expressed as:

$$\bar{a}_k = -\sum_{k=1,2}\mu_k\left(\frac{\bar{x} - \bar{x}_k}{|\bar{x} - \bar{x}_k|^3} + \frac{\bar{x}_k}{\bar{x}_k^3}\right) \tag{20}$$

Where $\vec{x}_k$ is the position vector of the third body gravitational perturbations of the Sun and Moon (k = 1 and 2), μ_k is the gravitational constant of third body gravitational perturbations of the Sun and Moon (μ_1 =1.32712438$\times 10^{20}$ m^3/s^2 and μ_2 = 4.902794$\times$ 10^{12} m^3/s^2 respectively).

3.1.1 Solar radiation pressure for cannonball model

The cannonball model (Pavlis et al., 1998), is assumed to be a reflective, uniform sphere, thus the attitude motion can be ignored and the acceleration due to the solar radiation pressure is given by:

$$\vec{a}_{can} = -\frac{A_{sphere}}{M}\frac{E}{c}\frac{A_{\oplus}^2}{|\vec{x}-\vec{x}_1|^2}\cdot\left(1+\frac{4}{9}C_d\right)\hat{S} \tag{21}$$

where A_{sphere} is the cross-section area of a sphere, C_d is the diffuse reflectivity coefficient. The surface normal unit vector, $\hat{S}$, is the unit vector in the direction of the Sun, E is the solar constant (1,353 W/m^2), c is speed of light (299,792,458 m/s), $A_{\oplus}$ is the astronomical unit (149,597,870 km).

3.1.2 Solar radiation pressure for non-spherical body

The solar radiation pressure, which is the largest non-gravitational perturbations in the geosynchronous region, depends on the area and its orientation with respect to the radiation coming from the Sun (Luthcke et al., 1997). For the rigid flat plate (j = 1 only), the solar radiation force can be expressed as:

$$\vec{F}_{SRP,j} = A_j\frac{E}{c}\frac{A_{\oplus}^2}{|\vec{x}_j-\vec{x}_1|^2}\hat{S}_j\hat{N}_j\left((1-C_{s,j})\hat{S}_j + 2(C_{s,j}\cdot\hat{S}_j\hat{N}_j + \frac{1}{3}C_{d,j})\hat{N}_j\right) \tag{22}$$

Thus, in case of the flexible model, the SRP acceleration of each lump mass of jth rod ($\vec{a}_{SRP,m_j}$ $\vec{a}_{SRP,m_{j+1}}$) in Fig 10 can be defined as:

$$\vec{a}_{SRP,m_j} = \vec{a}_{SRP,m_{j+1}} = \vec{a}_{SRP,j}/2 = \left(\frac{\vec{F}_{SRP,j}/2}{m_i}\right) \tag{23}$$

where A_j is the cross sectional area of the jth rod (j = 1 ,2), m_i is the mass of the jth and $j+1$th lump mass and $C_{s,j}$, $C_{d,j}$ and $C_{a,j}$,are the coefficients for specular, diffuse reflectivity and absorption for the jth rod respectively. The surface normal unit vector($\hat{N}_j$) and the solar incidence unit vector($\hat{S}_j$) are required to specify the orientation of debris on the centre of pressure of the jth rod.
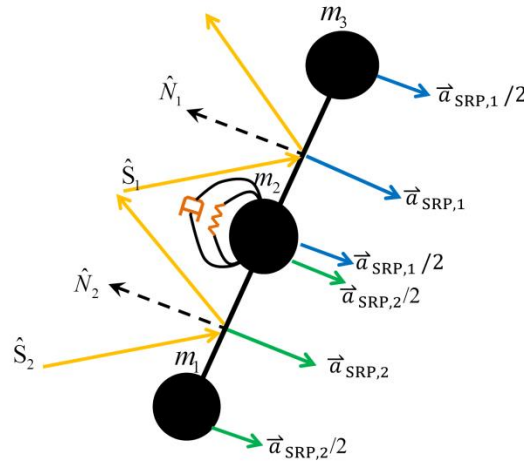

Fig 10 Solar radiation pressure on each lump mass of the flexible model in side view.

3.1.3   Average solar radiation pressure for flat rigid debris

For the flat rigid debris, the average SRP force over the possible tumbling motion is considered and this averaged force is then propagated. The attitude motion is one of causes to alter the effects of solar radiation pressure due to the changing size of the effective cross-sectional area. The benefits of this approach are to reduce computational cost by decoupling attitude and orbital dynamics.

In order to model a tumbling piece of debris, we can assume that any orientation in the inertial space will have equal probability of occurring. Therefore, the average force is obtained by integrating over the latitude and longitude of the Sun and setting $\hat{S} = [1, 0, 0]$. It is useful to integrate in terms of a spherical coordinate frame:

$$\vec{F}_{avg} = \frac{1}{4\pi} \int_0^\pi \int_0^{2\pi} \vec{F}_{SRP} d\lambda_s d\delta_s \qquad (24)$$

where a generic normal vector can be defined as:

$$\hat{N} = \begin{bmatrix} \cos\lambda_s \sin\delta_s \\ \sin\lambda_s \sin\delta_s \\ \cos\delta_s \end{bmatrix} \qquad (25)$$

However, the disadvantage of the spherical integration coordinates is that when we integrate over the two angles, the results is not a uniform distributions on the sphere surface but is concentrated at the pole, which may reduce some of the possible solar latitude and longitude values that effects the value of average SRP force (Weisstein, 2016). To fix this problem, we need to define the two angles (δ_s and λ_s) in the range on [0, 1] as a below transformation:

$$\bar{\lambda}_s = \frac{\lambda_s}{2\pi} \qquad (26)$$

$$\bar{\delta}_s = \frac{1 - \sin\delta_s}{2} \qquad (27)$$

Then, we differentiate Eq.(26) and Eq.(27):

$$d\lambda_s = 2\pi d\bar{\lambda}_s \qquad (28)$$

$$d\delta_s = -\frac{2d\bar{\delta}_s}{\cos\delta_s} \qquad (29)$$

We substitute Eq.(28)-(29) in Eq.(24) to calculate the average SRP force and the equivalent area is expressed as:

$$A_{eq} = \frac{\vec{F}_{avg}}{P_{SP}} \qquad (30)$$

Where $P_{SP} = \dfrac{E}{c}$ is solar radiation pressure per square metre.

Then, the average SRP acceleration can be calculated as:

$$\vec{a}_{AVG} = -\frac{A_{eq}}{M} P_{SP} \hat{\bar{S}} \qquad (31)$$

This average SRP of the flat rigid plate is studied in different scenario of perturbations (section 5.1 -5.2)

3.2   Attitude dynamics of the rigid flat plate model

Euler's rotational equations are the simplest method to compute the orientation of a rigid body at the centre of mass. The attitude dynamics of rigid body are given by:

$$\sum \bar{\tau} = I\dot{\bar{\omega}} + \bar{\omega} \times I\bar{\omega} \tag{32}$$

Where $\sum \bar{\tau}$ presents the summation of disturbance torques, I is the moments of inertia, $\bar{\omega}$ and $\dot{\bar{\omega}}$ is the angular velocity and acceleration respectively. In order to avoid any singularities, the kinematic attitude equations can be presented in terms of quaternions:

$$\dot{\bar{q}} = \frac{1}{2} \cdot \Omega \cdot \bar{q} \tag{33}$$

And $\Omega = \begin{bmatrix} 0 & \omega_3 & -\omega_2 & \omega_1 \\ -\omega_2 & 0 & \omega_1 & \omega_2 \\ \omega_2 & -\omega_2 & 0 & \omega_3 \\ -\omega_1 & -\omega_2 & -\omega_3 & 0 \end{bmatrix}$

Then, the solar radiation torque ($\bar{\tau}_{SRP}$) (Bohling et al., 1969) is determined as:

$$\bar{\tau}_{SRP} = \bar{\rho}_{SRP} \times (T \cdot \vec{F}_{SRP}) \tag{34}$$

Where $\bar{\rho}_{SRP} = \bar{\rho}_{com} + \bar{\rho}_{rad}$, $\bar{\rho}_{com}$ is the vector of the geometric centre of the object to the centre of mass, $\bar{\rho}_{rad}$ is the vector from the geometric centre of the object to the centre of pressure and T is the transformation matrix from the inertial frame to the body frame. The gravitational torque ($\bar{\tau}_{Grav}$) (Blackburn et al., 1969) is derived by the gravitational force acting on the debris from:

$$\bar{\tau}_{Grav} = \frac{3\mu}{x^3} \left[\hat{X} \times I\hat{X} \right] \tag{35}$$

Where $\hat{X} = T \cdot \hat{x}$ is the unit vector of the object transformed to the body frame. The attitude dynamics will be coupled with orbital dynamics and implemented in the Monte Carlo simulation (section 5.3) for the flat rigid plate.

3.3   Attitude representation of the flexible model

The flexible model can change shape and this leads to changes in the position of a centre of mass over time. Therefore, we determine the origin of body reference frame on the second lump mass as shown in Fig 11. The x-axis ($\vec{x}_b$) is the cross product between $\vec{r}_1$ and $\vec{r}_2$ are the positions of the end masses with respect to the middle in the Earth-centred inertial coordinates (ECI) frame. The y-axis ($\vec{y}_b$) is a unit vector between $\vec{r}_1$ and $\vec{r}_2$ by calculating the direction cosine of a half of the deformed angle ($\theta_d / 2$) and the z-axis ($\vec{z}_b$) is cross product between $\vec{x}_b$ and $\vec{y}_b$. We define the direction cosine matrix (3-1-3 sequence, (ψ, θ, ϕ)) (Schaub and Junkins, 2003). Then, we use the (3-1-3) Euler rotation matrix to calculate the attitude representation of the flexible model.
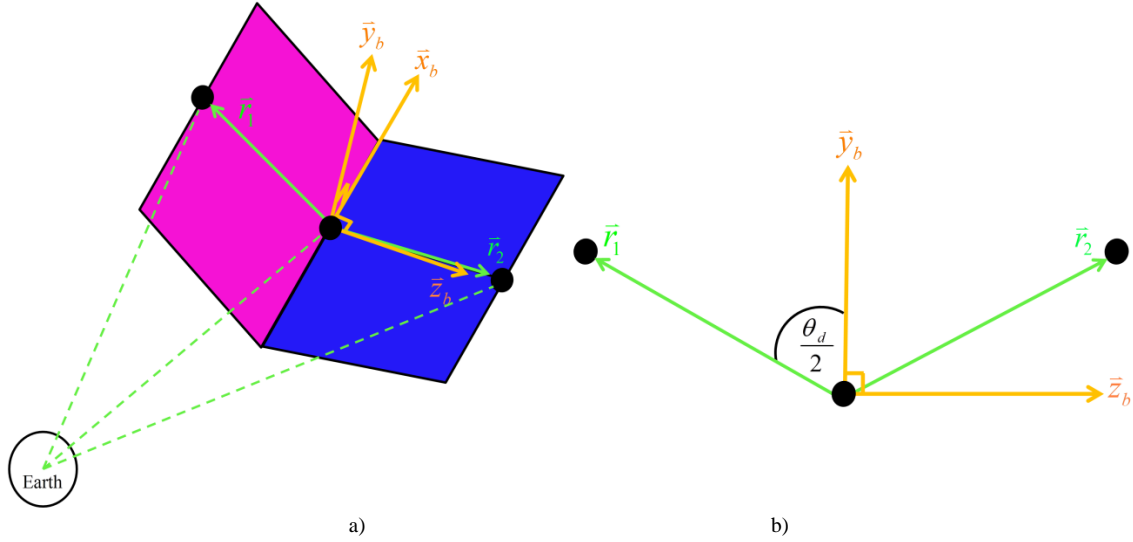
Fig 11 Representative of flexible model's attitude motion in body frame ($\vec{x}_b$, $\vec{y}_b$, $\vec{z}_b$) a) 3D in ECI frame b) 2D in the deformation plane

3.4 Self-shadowing effect of the flexible model

There are three main methods commonly used in real-time 3D computer graphics to represent shadowing effects. These are: planar shadow, shadow volume and shadowing mapping. In this work, the planar shadow method, first developed by Blinn (Blinn, 1988) is applied to generate shadows by projecting the shadow casting object's polygons onto a plane. This method is suitable to calculate self-shadowing of the flexible model because it is the easiest and fastest to implement and the flexible model has a simple geometry but the disadvantage is that a shadow cast on a plane does not create soft shadow (penumbra), which SRP force will not be nil because of partial illumination. In Fig 12, point $\vec{p}$ is the projection of each vertex $\vec{v}$ onto the plane P: $\vec{n}_p \cdot \vec{x}_p + d_p = 0$ due to a light source vector ($\vec{l}$). The shadow cast the on plane can be defined as:
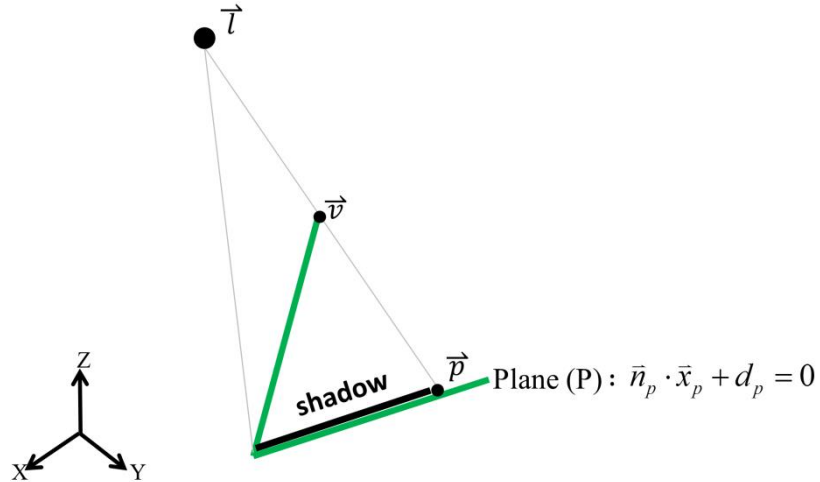

Fig 12 Planar shadow projection.

The shadow cast on plane can be defined as:

$$\bar{p} = \bar{l} - \frac{d + \vec{n} \cdot \vec{l}}{\vec{n} \cdot (\vec{v} - \vec{l})}(\vec{v} - \vec{l})$$

(36)

This can be written into a projection matrix ($\bar{p} = M\vec{v}$) (Eisemann et al., 2012).

$$M = \begin{bmatrix} \vec{n} \cdot \vec{l} + d - l_x n_x & -l_x n_y & -l_x n_z & -l_x d \\ -l_y n_x & n \cdot l + d - l_y n_y & -l_y n_z & -l_y d \\ -l_z n_x & -l_z n_y & n \cdot l + d - l_z n_z & -l_z d \\ -n_x & -n_y & -n_z & \vec{n} \cdot \vec{l} \end{bmatrix} \qquad (37)$$

The self-shadowing algorithm has two main steps. Firstly, it performs a check to determine which plane, if any, casts a shadow on the other. The vector from the Sun to the centre of mass of the plane will determined which plane is closer to it. The algorithm then determines if an area of the plane is exposed to SRP by checking the intersection between the shadow and the plane. In case of the non-intersection, SRP forces of both planes are normally calculated. This algorithm is calculated at each integration step.

Fig 13 (a) presents a self-shadowing simulation test. The topmost plane acts as a shading plane. The bottom plane has a shadow cast upon its surface. The light source is at coordinates (5, 1, 4). The shaded area depends on the position of the light source and the object's shape. Fig 13(b) and Fig 13(c) show different shadows created by moving the light source coordinates to (5, -1, 2) and (-1, 0, 4.5) as well as the changing the orientation of the object. It can clearly be seen that different orientations and relative positions cause significant changes in the solar radiation pressure on a shaded plane.
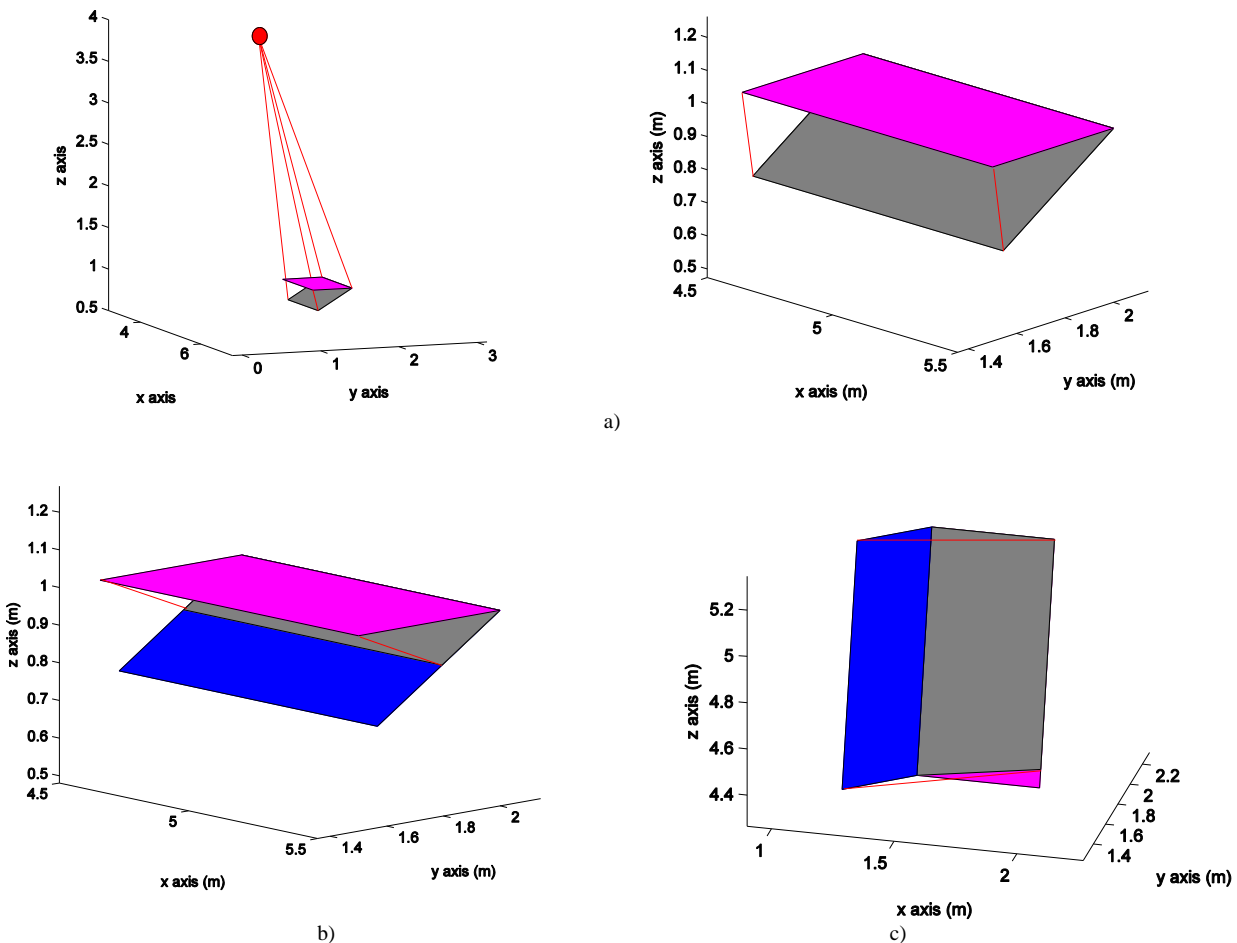

a)

b)

c)

Fig 13 Self-shadowing area simulations a) light source (5,1,4) above the model and full shadow on the second plane b) shadow area after moving light source position down at (5,-1,2) c) shadow area after rotating and light source position (-1, 0, 4.5).

4. SIMULATION ANALYSIS

Two different kinds of MLI (Sheldahl, 2012) are selected for analysis: PET® and Kapton®. PET® (perfect reflection properties) is coated aluminium on both sides while Kapton® is coated only on one side (imperfect reflection properties) as shown in Fig 14 and Table 1. There are three body model types considered for these investigations: cannonball, flat rigid plate and flexible model to investigate the orbital dynamics of each. The cannonball objects represent as reference object and we define the same AMR value and same reflection properties in Table 1. The initial geometries of both flat rigid plate and flexible model are assumed to be that of a flat plate (Fig 14). In this paper, we propagate the orbits from January 1, 2012. All objects start with the same set of Keplerian elements as shown in Table 2. Fig 15 shows the initial position of debris, the Sun and the Moon positions in ECI frame. Initial Euler angles measured at the second lump mass that is assumed to be the origin of body frame of reference are chosen to be 50, 9 and 85 degrees respectively and the initial angular velocity set to zero for all components. The numerical integration used to solve the propagation of the differential equations in this study is the Runge-Kutta method (ODE45) in MATLAB® : RelTol: 1.0×10^{-8} ,AbsTol: 1.0×10^{-8} to protect a big change in orbit and attitude motion of HAMR object due to the perturbations, especially SRP. We choose to fix a time interval step at: 1 second of each integration ($t_0 = t_{initial}$:1:t_{final}) instead of a step size in the option of ODE45 because it is possible to miss points where the step size frequency is greater than the solver's frequency.
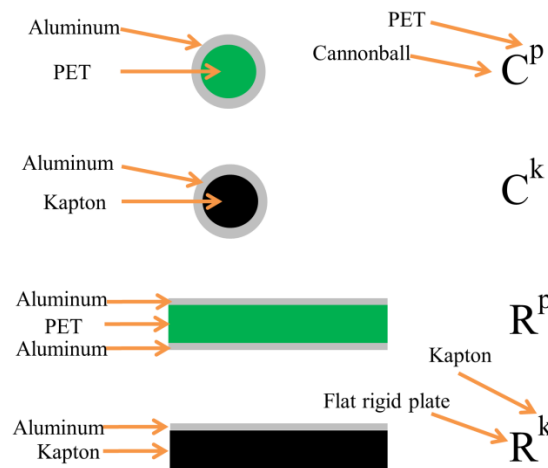

Fig 14 Cross-sectional objects of cannonball model and flat rigid object.

Table 1 Properties of PET and Kapton (Sheldahl, 2012).

Material type		AMR (m²/kg)	Young's Modulus (N/m²)	Cs, Cd, Ca	k_s (N·m/rad)	c_s (N·m·s/rad)
PET	Coated	111.11	8.81×10^9	0.60 0.26 0.14	0.0043	1.2388E-05
Kapton	Coated	26.30	2.50×10^9	0.60 0.26 0.14	0.0051	1.3904E-05
	Uncoated	26.30		0.00 0.10 0.90		

Table 2 Initial orbital elements.

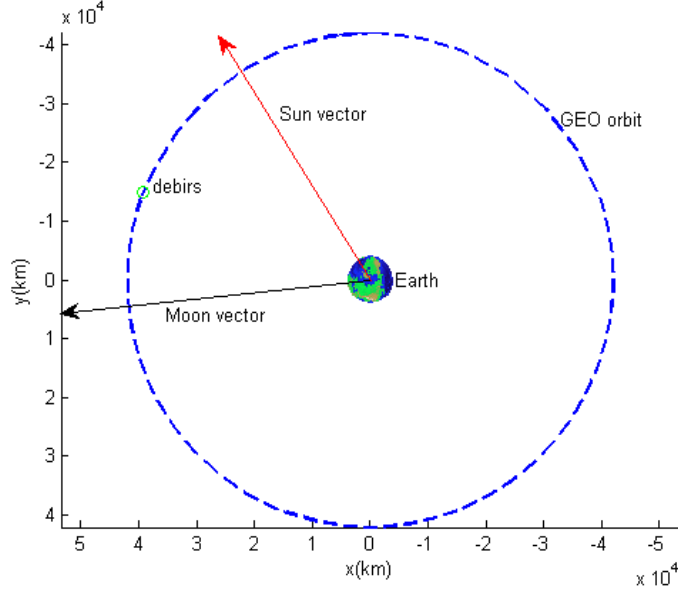| Keplerian element	
Semi-major axis (km)	42,184
Eccentricity	0.0001
Inclination (degrees)	5.0
Argument of perigee (degrees)	9.0
Longitude of ascending node (degrees)	30.0
Mean anomaly (degrees	270.0

Fig 15 The Sun, Moon and debris vectors in ECI frame on January 1, 2012.

The orbital and attitude evolutions of all debris models have been investigated under selected perturbation regimes. Simulations considering the J_2 perturbation only are labelled with the subscript "j", those with third body gravitational perturbations from the Sun and the moon are labelled with subscript "g", while SRP force is indicated by subscript "s". Self-shadowing, considered only in the case of the flexible model is denoted by subscript "h". The capital letters "C", "R", "RC" and "M" indicate the cannonball model, flat rigid body with average SRP, flat rigid body with coupled attitude and orbital motions and flexible body respectively. The material of the model is labelled with superscript "p" and "k" for PET® and Kapton® respectively. The summary of the objects and their characteristics used in the numerical simulations is shown in Table 3. A combination of the subscripts indicates which models/materials/perturbations are considered case by case.

Table 3 Summary of letters to describe simulated objects.

Model	Letter	Material	Superscript	Perturbations	Subscript
Cannonball	C	PET	p	J_2	j
Flat rigid plate with average SRP	R	Kapton	k	Third body	g
Flat rigid plate coupled attitude and orbital motions	RC			SRP	s
Flexible model	M			Self-Shadow effect	h

5. RESULTS AND DISCUSSION

In this section, we present and discuss the evolution of the attitude dynamics and orbital parameters of the flexible model and compare that with the flat rigid plate and cannonball model (reference object) for two material types (PET® and Kapton®) over a period of 12 days. In order to analyse the effects of each perturbation, we investigate three scenarios: J_2 and SRP, gravitation (J_2 and third body) and lastly all perturbations combined. All investigations are simulated with a PC with Intel Core7@ 1.80 GHz with 8 GB of RAM. The comparison of the integration time for one-day evolution of each model and relative results of flexible model by varying the tolerance (RelTol and AbsTol: 10^{-8}, 10^{-10}, 10^{-12} and 10^{-14}) are presented in Fig 16 and Fig 17. The computational cost of the flexible model in Fig 16 takes longer (tolerance: 10^{-14} requires 12,302.32 seconds (3 hours 25 minutes)/day) than cannonball and rigid flat plate due to coupled orbit and attitude dynamics. The percent of relative error in Fig 17 presents that the percent errors of the flexible model increase when the tolerance is tighten (the maximum error of each tolerance: 10^{-10}, 10^{-12} and 10^{-14} are 0.26%, 0.61%

and 0.74% respectively) while the maximum error of both cannonball and rigid flat plate of each tolerance are in range of 10^{-7}%. It is because of a slightly different change of a shape (deformation and self-shadowing) that results in a significantly different orbital dynamics. Therefore, tighter tolerance can significantly improve the propagation accuracy for the flexible model because of the stiffness of the problem but the computational time required might become extremely high. Due to our resource limitations, we therefore choose to simulate all investigations at tolerance: 10^{-8} in this paper.

a)

b)
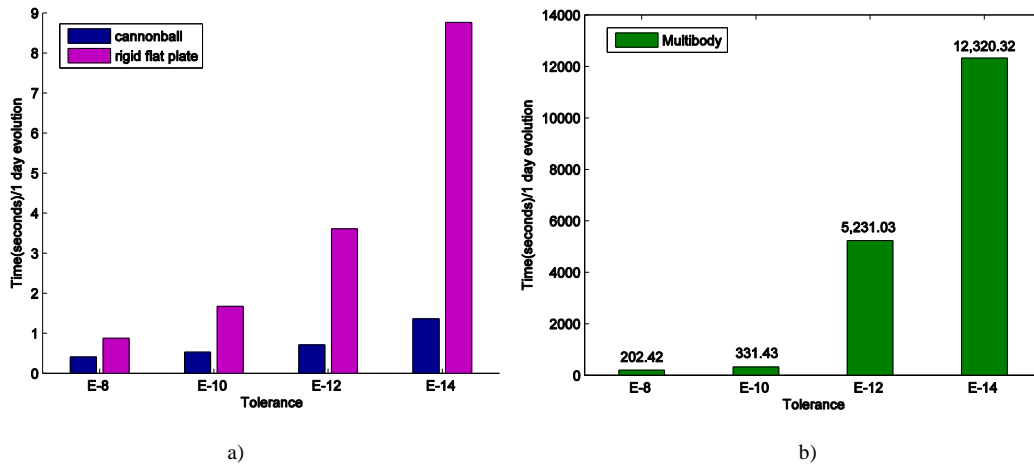
Fig 16 Comparison of integration time of each model by varying the tolerance (RelTol and AbsTol) over a 1-day evolution.
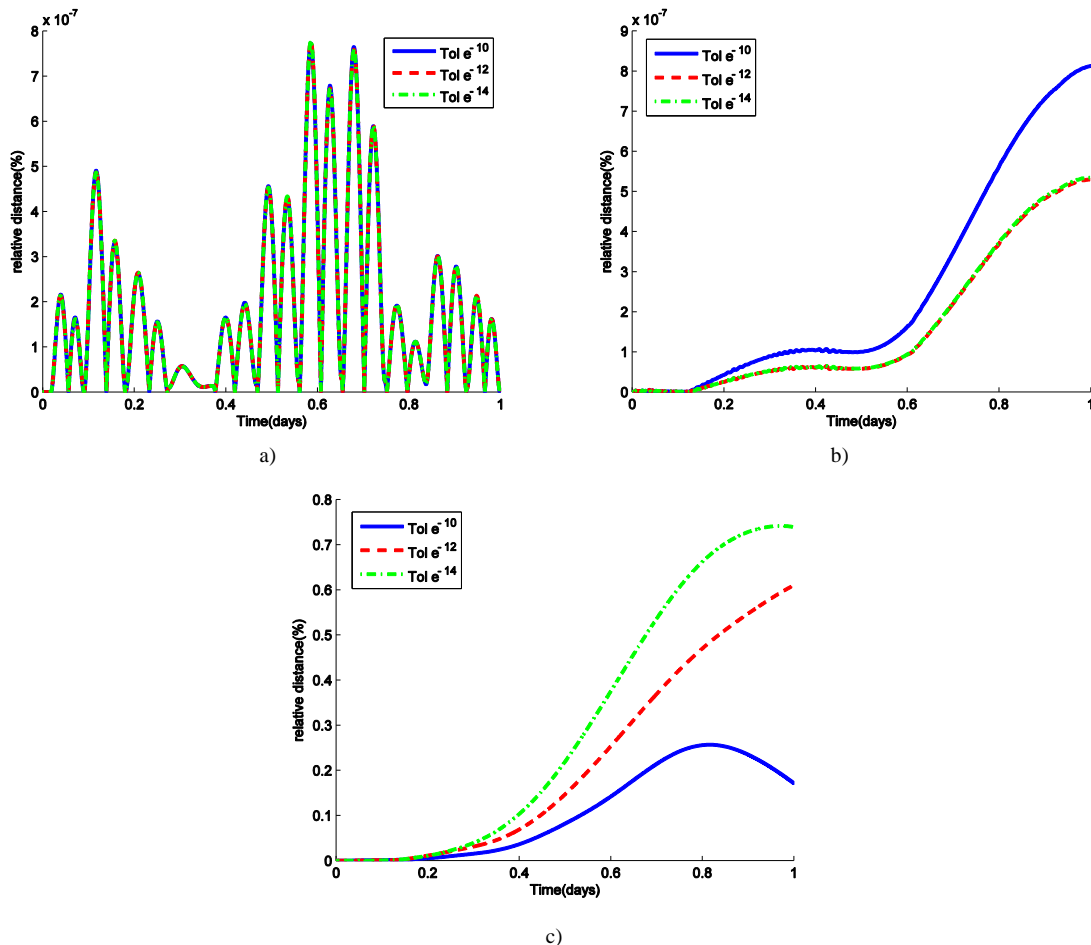

a)

b)

c)

Fig 17 Comparison of the relative error of each model by comparing the results of tolerance: 10^{-8} of orbital positions over a 1-day evolution by varying the tolerance (RelTol and AbsTol): 10^{-8}, 10^{-10}, 10^{-12} and 10^{-14} a) cannonball b) rigid flat plate c) flexible model.

In order to understand the effects that different attitude positions and object shape in section 5.3 (Monte Carlo simulation) have on the orbital evolution we run Monte Carlo simulations with 500 different initial conditions that are run on a Linux-based parallel computing cluster (each node: Dual 2 core AMD Opteron 2214 with 4 GB) that computational cost of the flexible model is 8.26 hrs/one day evolution.

5.1   Dynamics under J₂ and solar radiation pressure

Fig 18 shows the dynamical evolution for the PET® over 12 days for four different scenarios: M_{js}^{p}, M_{jsh}^{p}, R_{js}^{p} and C_{js}^{p}. The variations of the orbital elements are significantly different for each object. Both eccentricity of M_{js}^{p} and M_{jsh}^{p} lie between C_{js}^{p} and R_{js}^{p} while the inclination of C_{js}^{p} show the largest amplitudes in variations of inclination. It can be seen that the inclination of M_{js}^{p} and M_{jsh}^{p} present almost similar periodic behaviours. The reason for this is that the SRP accelerations of flexible model depends on variations of the effective cross-section area throughout the orbital revolution due to tumbling and self-shading effect while the SRP accelerations of both rigid bodies are caused only by the varying distance to the Sun, which does not significantly change in the short period of the simulation.

In the same simulation with Kapton® (M_{js}^{k}, M_{jsh}^{k}, R_{js}^{k} and C_{js}^{k}), Fig 19 shows that the orbital evolutions of C_{js}^{k} exhibits the highest secular trend in eccentricity and the largest amplitude in variations of the inclination. It is, therefore, worthy to note that the cannonball model is not suitable to approximate the orbital motion of an object with imperfect reflection properties. The inclination evolutions of M_{js}^{k} and M_{jsh}^{k} are larger than R_{js}^{k} due to variations in the effective cross sectional area of the flexible model as the previously mentioned for the case of PET®. Comparing both material types for the flexible model, the evolutions of Kapton® are obviously smaller due to AMR, which is around 5 times lower and its imperfect reflection properties.
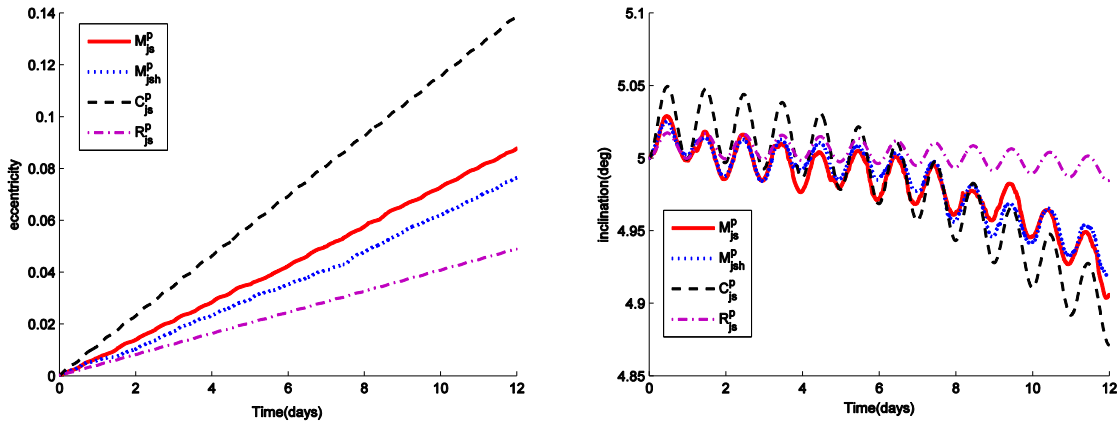

Fig 18 Comparison of eccentricity and inclination evolution of M_{js}^{p}, M_{jsh}^{p}, R_{js}^{p} and C_{js}^{p} under J₂ and solar radiation pressure over 12 days.
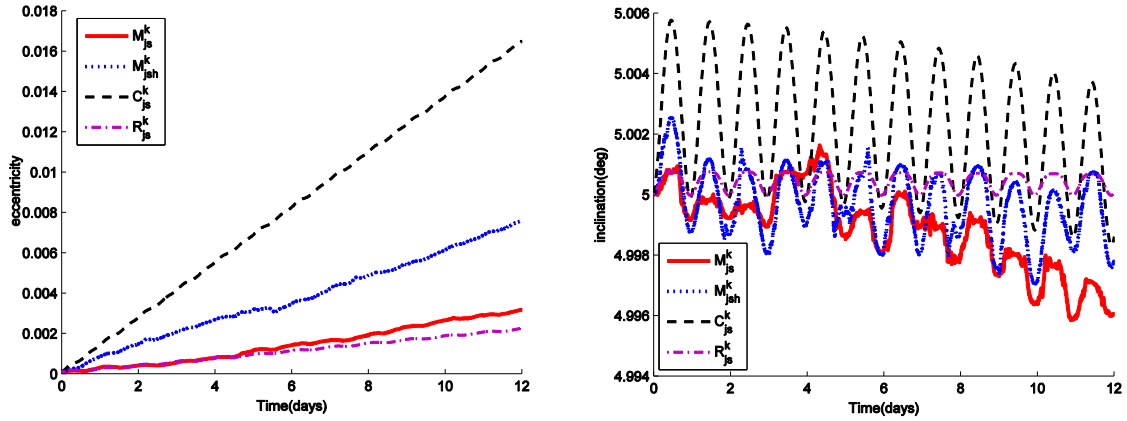
Fig 19 Comparison in eccentricity and inclination evolutions of M_{js}^{k}, M_{jsh}^{k}, R_{js}^{k} and C_{js}^{k} under J$_2$ and solar radiation pressure over 12 days.

5.1.1 *Physical dynamics of the flexible model over 10 minutes*

In order to better understand the dynamics of the flexible model, we restrict the time of the investigation to 10 minutes and start from the same initial positions and velocities of M_{js}^{p} on the 2nd day in the previous propagation and the same initial configuration in Fig 20 (deformed angle: 30 degrees) for both PET® and Kapton®. Fig 21(a) shows the physical dynamics of M_{js}^{p} without considering the self-shadowing effect. In this case, the absolute accelerations of both planes (M_{js}^{p}) in Fig 21(b) does not reach zero. Comparing with the evolution of M_{jsh}^{p} in Fig 22(a), we can notice that the self-shadowing effect leads to different deformation and tumbling when compared to M_{js}^{p}. The first plane, M_{jsh}^{p} is not exposed to direct solar radiation pressure due to self-shadowing effect and the overall absolute accelerations of both planes in Fig 22(b) shows null or small accelerations. The rotations of M_{js}^{p} is different when compared to the rotations of M_{jsh}^{p} as shown in Fig 21(c) and Fig 22(c) respectively. Self-shading effect causes both different deformations and unique, rapid, non-stable attitude motion of M_{js}^{p} and M_{jsh}^{p}. This is due to the fact that self-shadowing reduces the amount of SRP acting one side of the plate leading to a difference in the force vectors between the two sides.
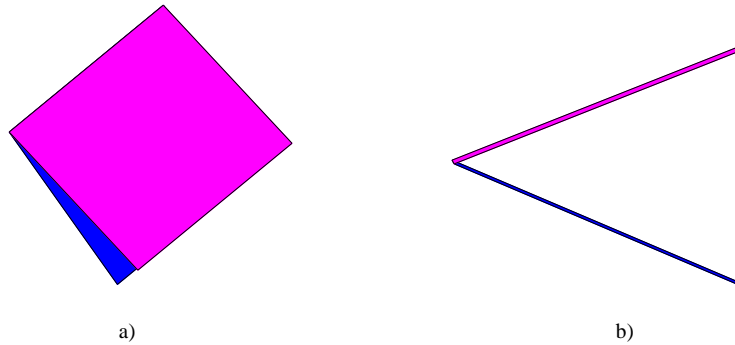

a)   b)

Fig 20 Initial geometry of PET® of investigation in 10 minutes under J$_2$ and solar radiation pressure a) 2D view b) side view.
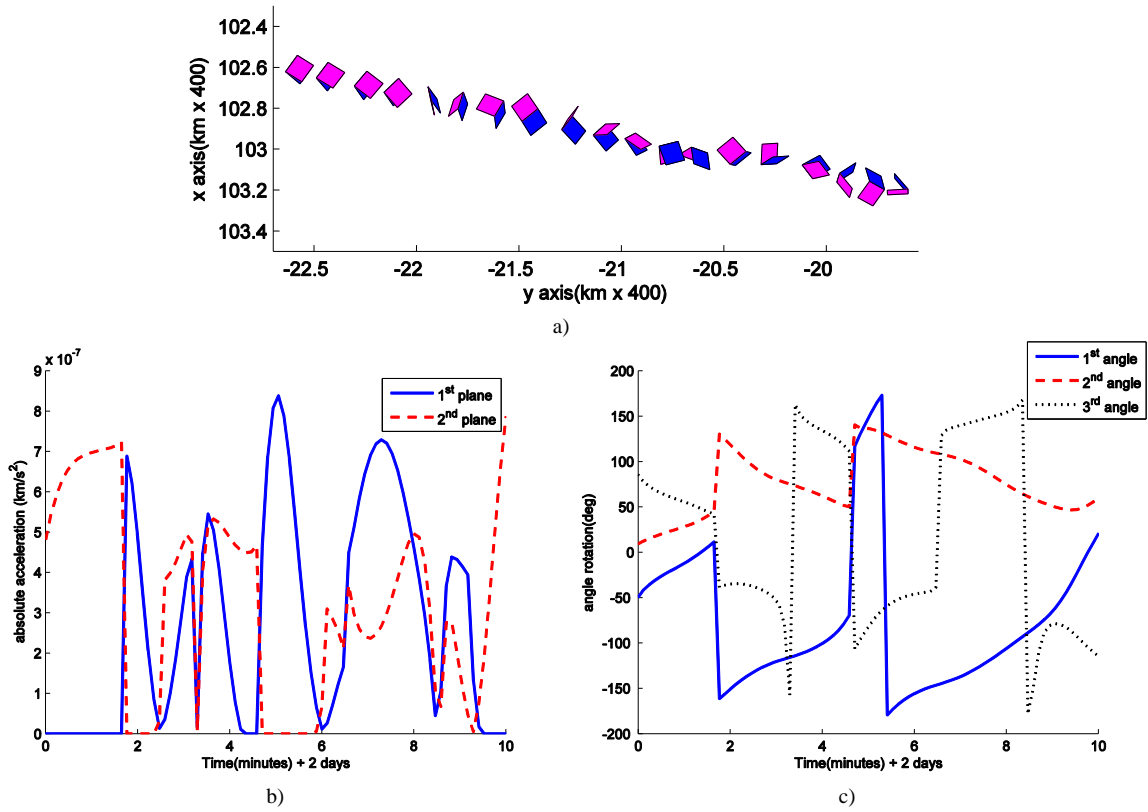
Fig 21 PET® under J$_2$ and solar radiation pressure without self-shadowing (M_{js}^p) in 10 minutes a) time-lapse of deformation in the inertial frame (1 line/ 30 seconds) b) absolute acceleration of both planes c) Euler angle evolution.
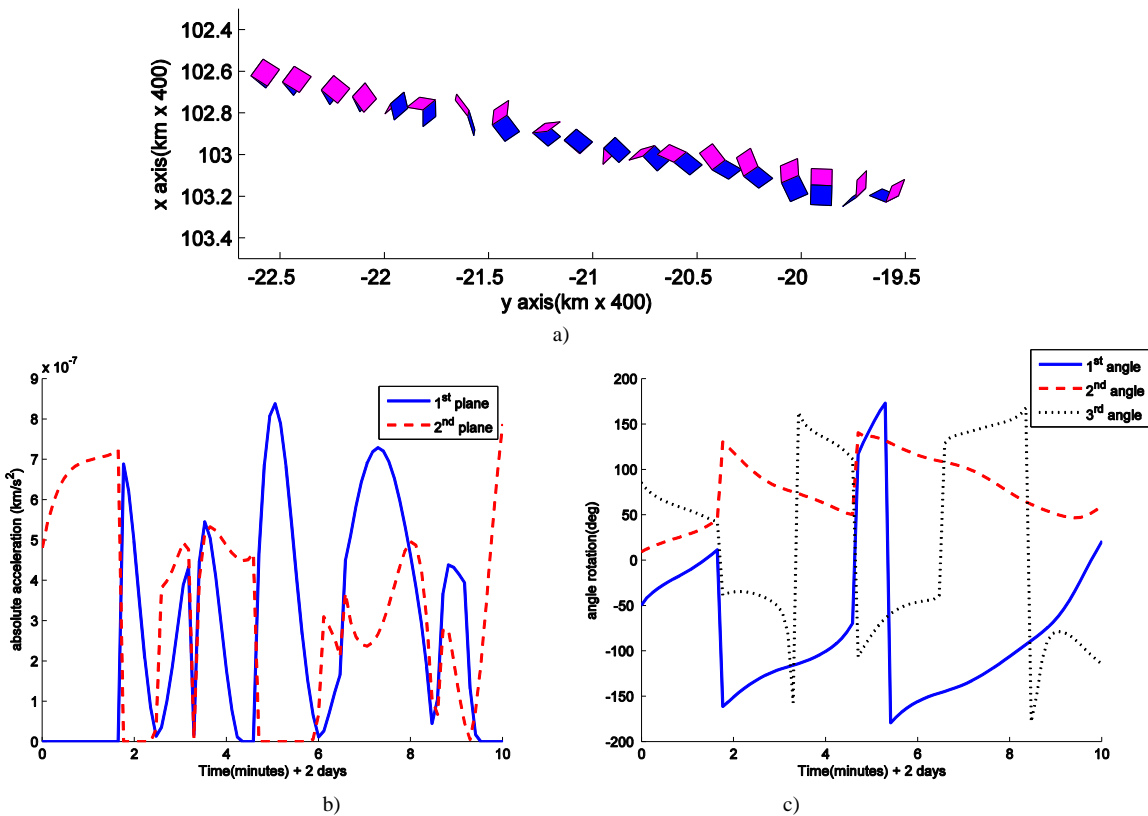

Fig 22 PET® under J$_2$ and solar radiation pressure with self-shadowing (M_{jsh}^p) in 10 minutes a) time-lapse of deformation in the inertial frame (1 line/ 30 seconds) b) absolute acceleration of both planes c) Euler angle evolution.

The analysis of the motion of Kapton® model under the effects of J_2 and SRP over a period of 10 minutes is shown in Fig 23 and Fig 24. Due to the non-uniform reflection properties of Kapton®, the front surface is coated with highly reflective aluminium while the back side does not have any coating and hence has significantly lower reflectivity. There are three possible scenarios for the perturbations forces acting on the model. Firstly, the SRP acts on the aluminium-coated surfaces and the object moves subject to both SRP and J_2 perturbations. Secondly, if SRP acts on the uncoated sides then the motion of the object is dominated by J_2 perturbation rather than SRP. Lastly, on the shape when folded on the hinge, the solar radiation pressure hits two different surface normals and will result in a different acceleration, independently of the coating. This leads to the deformation of the geometry and rotations as shown in Fig 23(a). This mechanism is similar to the self-shadowing effect. Comparing the absolute acceleration of both M_{js}^{k} and M_{jsh}^{k}, the complete shading plane (M_{jsh}^{k}) on the first plane in Fig 24(b) is found at the start due to zero absolute acceleration as initial conditions while M_{js}^{k}, shows that SRP forces acts on both planes. These mechanisms of self-shadowing are as similar to the case of PET® in the previous case study.

To summarise, the short term period analysis of both PET® and Kapton®, the self-shadowing causes a variation in the SRP forces acting on the body which results in different deformations and tumbling of the flexible model when compared to the results without considering self-shadowing effects. The rotation of M_{jsh}^{p} is, however, faster than M_{jsh}^{k} due to smaller areal density and uniform reflection properties.
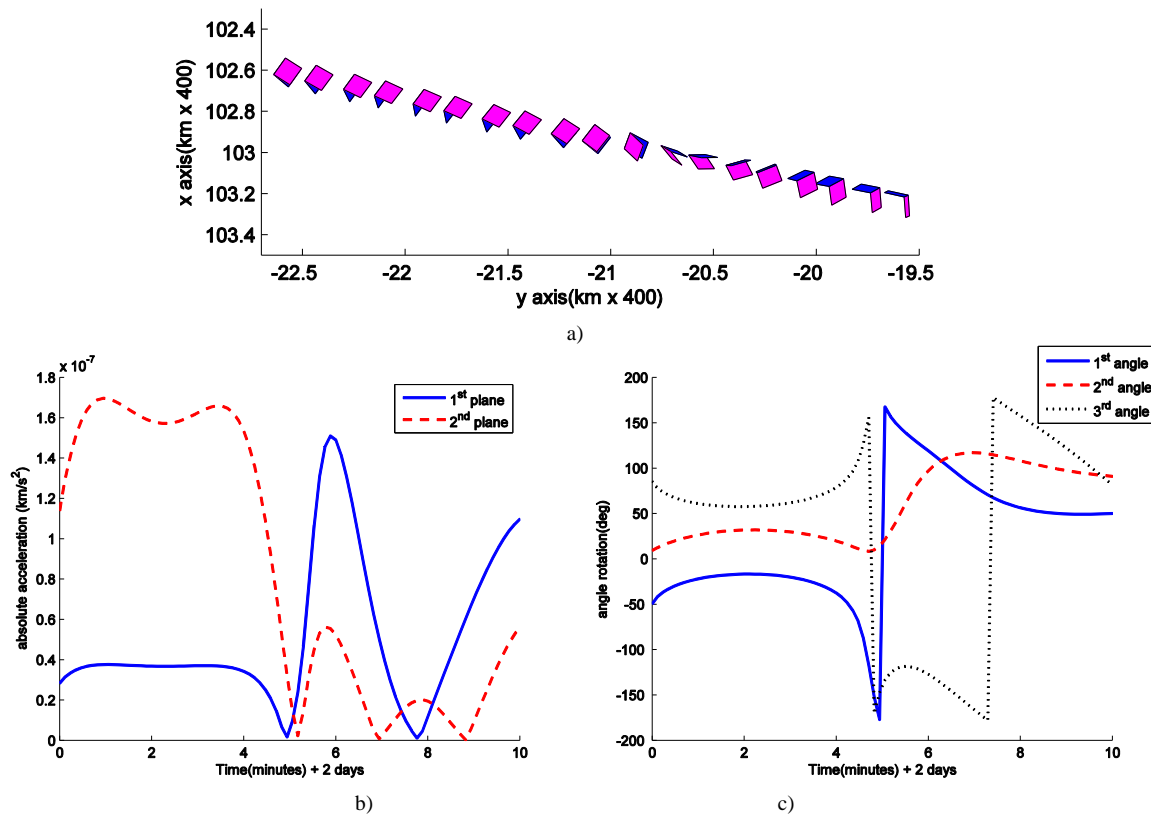

Fig 23 Kapton® under J_2 and solar radiation pressure without self-shadowing (M_{js}^{k}) in 10 minutes a) time-lapse of deformation in inertial frame (1 line/ 30 seconds) b) absolute acceleration of both planes c) Euler angle evolution.
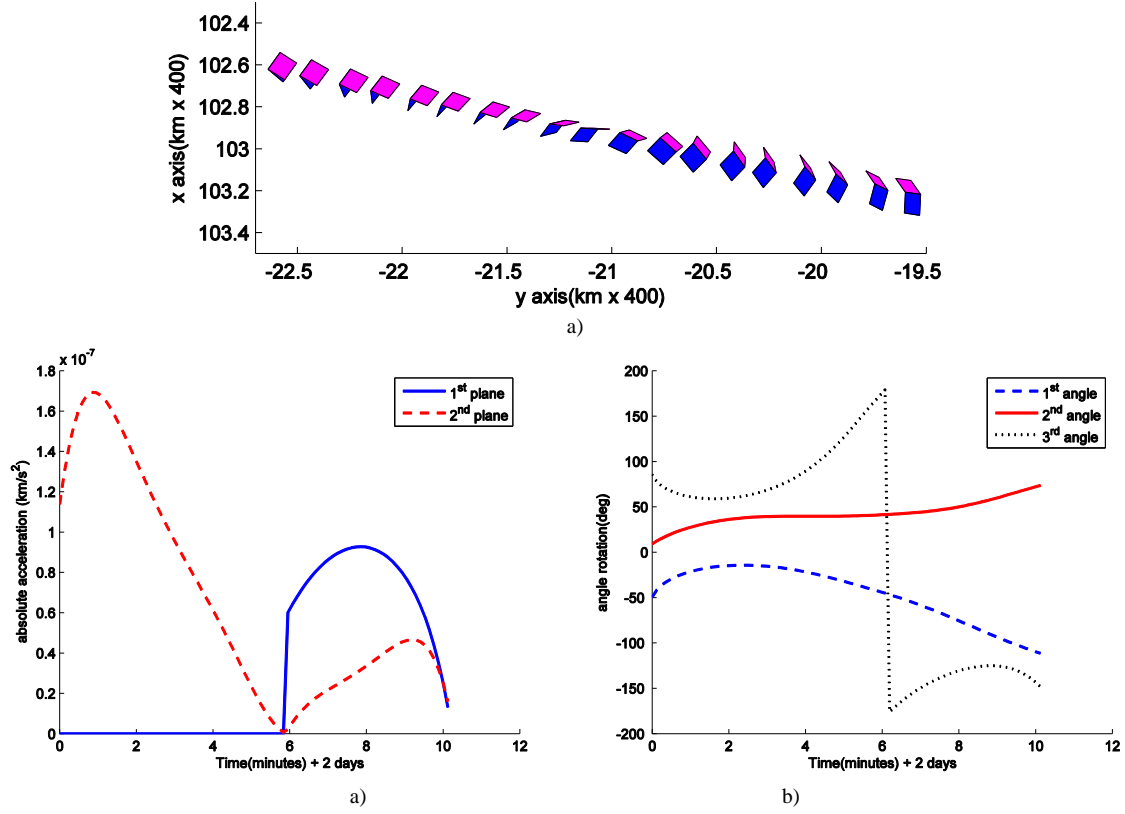
Fig 24 Kapton® under J_2 and solar radiation pressure with self-shadowing (M_{jsh}^k) in 10 minutes a) time-lapse of deformation in inertial frame (1 line/ 30 seconds) b) absolute acceleration of both planes c) Euler angle evolution.

The change in cross sectional area mainly alters the effect of the solar radiation pressure leading to changes in the object's attitude. Fig 25(a) and Fig 25(b) show the propagations of effective cross-section area over a period of 10 minutes of PET® (M_{js}^p , M_{jsh}^p and R_{js}^p) and Kapton® (M_{js}^k , M_{jsh}^k and R_{js}^k) under J_2 and SRP disturbances. The effective cross-section areas of the rigid model (R_{js}^p and R_{js}^k) are calculated by averaging all possible attitudes of effective area over solar latitude and longitude leading to both average exposed area values of 0.1713 m² and 0.1010 m² respectively. The equivalent area of R_{js}^k is around 0.58 times the equivalent area of R_{js}^p due to imperfect reflection properties. For the flexible model, the effective cross-section areas are the summation of the effective cross-section area of both planes due to their rotations.

Analysing the effects of self-shadowing in Fig 25, it can be seen that the effective cross-sectional area with self-shadowing differs significantly from that with non-self-shadowing for both PET® and Kapton®. The rate of change of the effective cross-section area of M_{js}^p and M_{jsh}^p in Fig 25(a) fluctuates more rapidly than that of M_{js}^k and, M_{jsh}^k in Fig 25(b). The highest value of effective cross-sectional area indicates that the SRP vector acts almost perpendicularly to the debris plane while the lowest value corresponds to the debris plane being almost parallel to SRP vector. These results are in accordance with the unstable attitude motion and variations in SRP accelerations discussed in previous section.
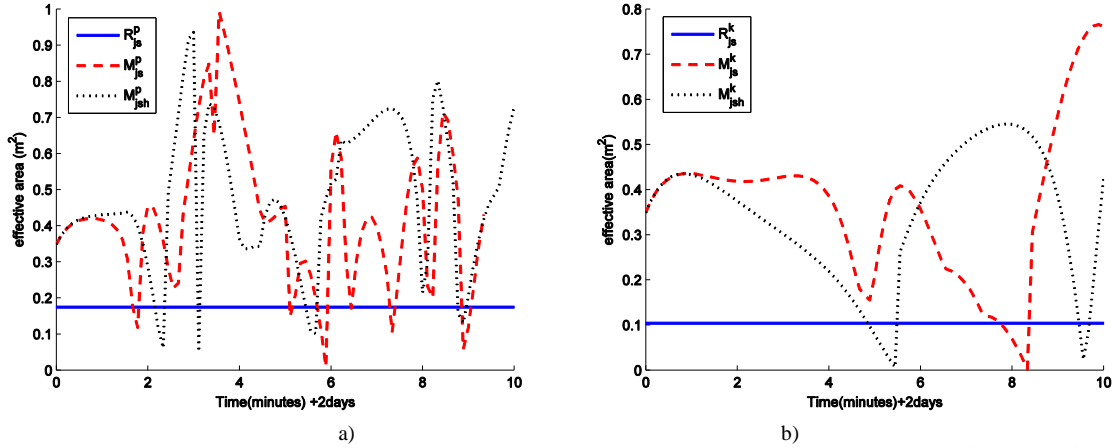
a)   b)

Fig 25 Variation of effective cross-section area under J_2 and solar radiation pressure in 10 minutes a). PET® b) Kapton®

Fig 26(a) and Fig 26(b) show that there are very small changes in both inclination and eccentricity of M_{jg}^{p}, R_{jg}^{p}, M_{jg}^{k} and R_{jg}^{k}. Fig 26(c) and Fig 26(d) shows the difference in inclination and eccentricity of both materials in the order of 10^{-5} and 10^{-8} respectively when applied to the flat rigid plate model. While the changes for the eccentricity appear to be bounded, the inclination change suggests a secular trend. It would suggest that the J_2 and third body effects insignificantly affect the orbital dynamic of the flexible model when compared to the cannonball. For the simulation of the deformation dynamics, Fig 27 shows the spin of M_{jg}^{p}. The cause for this behaviour is that the gravity gradient torque acts differently on each lump mass. This leads to the deformation of the body and the ensuing tumbling motion (Fig 27(b) - Fig 27(c)).
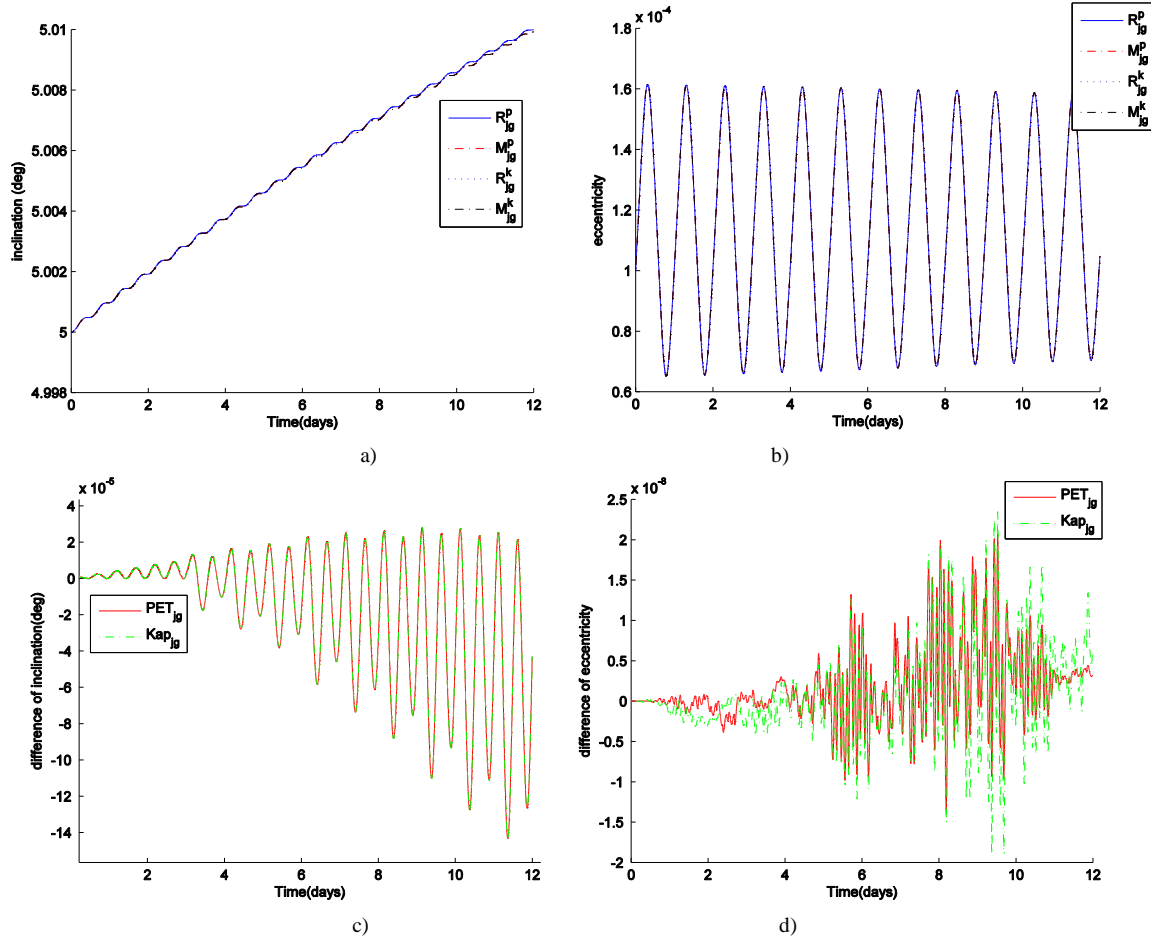
a)

b)

c)

d)

Fig 26 Inclination and eccentricity evolution of M_{jg}^{p}, R_{jg}^{p}, M_{jg}^{k} and R_{jg}^{k} under J$_2$ and third body perturbations over 12 days a). Inclination evolution b) Eccentricity evolution c) Difference in inclination between flexible model and rigid models d) Difference in eccentricity between flexible and rigid model.
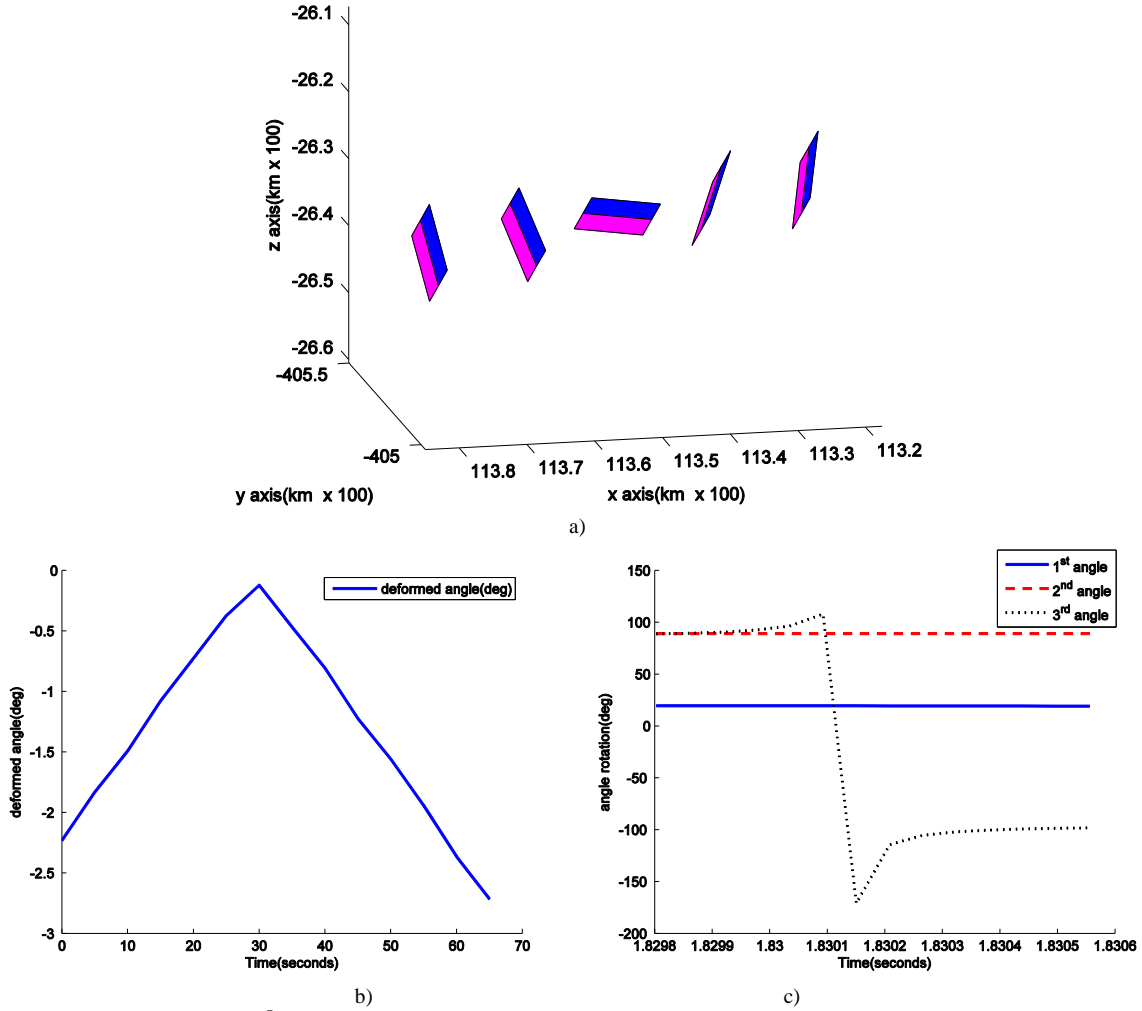
Fig 27 Tumbling and deformation of PET® object under J₂ and the third body from the Sun and Moon during 1.8296-1.8305 day (65 seconds) a) Time-lapse of deformation in inertial frame (1 line /3 seconds) b) Deformation angle evolution c) Euler angles evolution.

5.2 Dynamics under all perturbations

This section aims to investigate the orbital evolution under the effects of all perturbations for the three objects (M_{jgsh}^{p}, M_{jgsh}^{k}, R_{jgs}^{p}, R_{jgs}^{k}, C_{jgs}^{p} and C_{jgs}^{k}) over a period of 12 days with the self-shadowing effect considered for the flexible models (M_{jgsh}^{p}, M_{jgsh}^{k}). Fig 28 shows the orbital dynamics of the bodies. C_{jgs}^{p} presents the highest variations in both inclination and eccentricity. The maximum inclination change of M_{jgsh}^{p} can reach $\Delta i \approx 0.033$ while for M_{jgsh}^{k}, this is one order of magnitude smaller at around $\Delta i \approx 0.006$. The difference is due to PET® being lighter than Kapton® and having uniform reflection properties. It is evident from these results that the variations in both inclination and eccentricity caused by SRP are dominant over those exerted by J₂ and the third body from the Sun and Moon. The angular velocities of M_{jgsh}^{p} and M_{jgsh}^{k} during 3.0-3.3 day are shown in Fig 29 and Fig 30 respectively and both display very fast and complex motion. It is worthy to note that the combinations of the flexible model, reflection properties and the self-shadowing effect lead to unique non-stable rotations and deformations of both PET® and Kapton®.
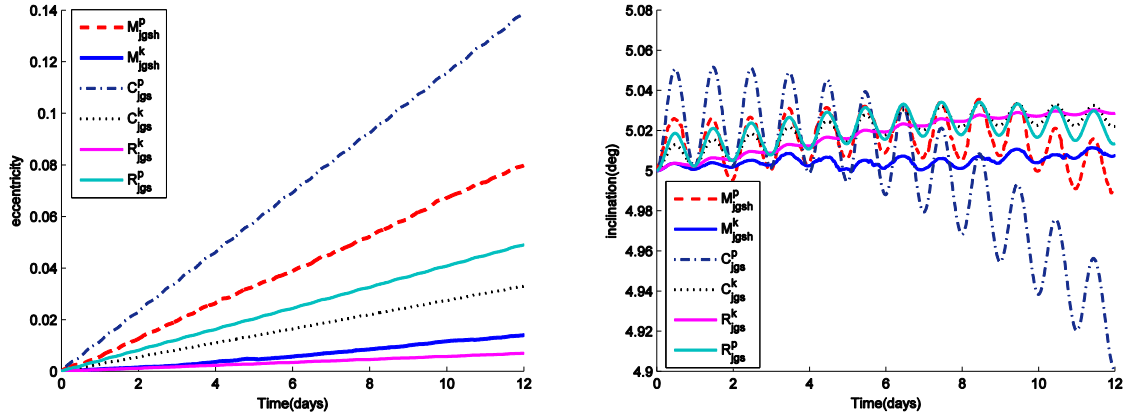
Fig 28 Comparison in eccentricity and inclination evolution over 12 days of M^p_{jgsh}, M^k_{jgsh}, R^p_{jgs}, R^k_{jgs}, C^p_{jgs} and C^k_{jgs} under J_2, third body perturbations and solar radiation pressure.
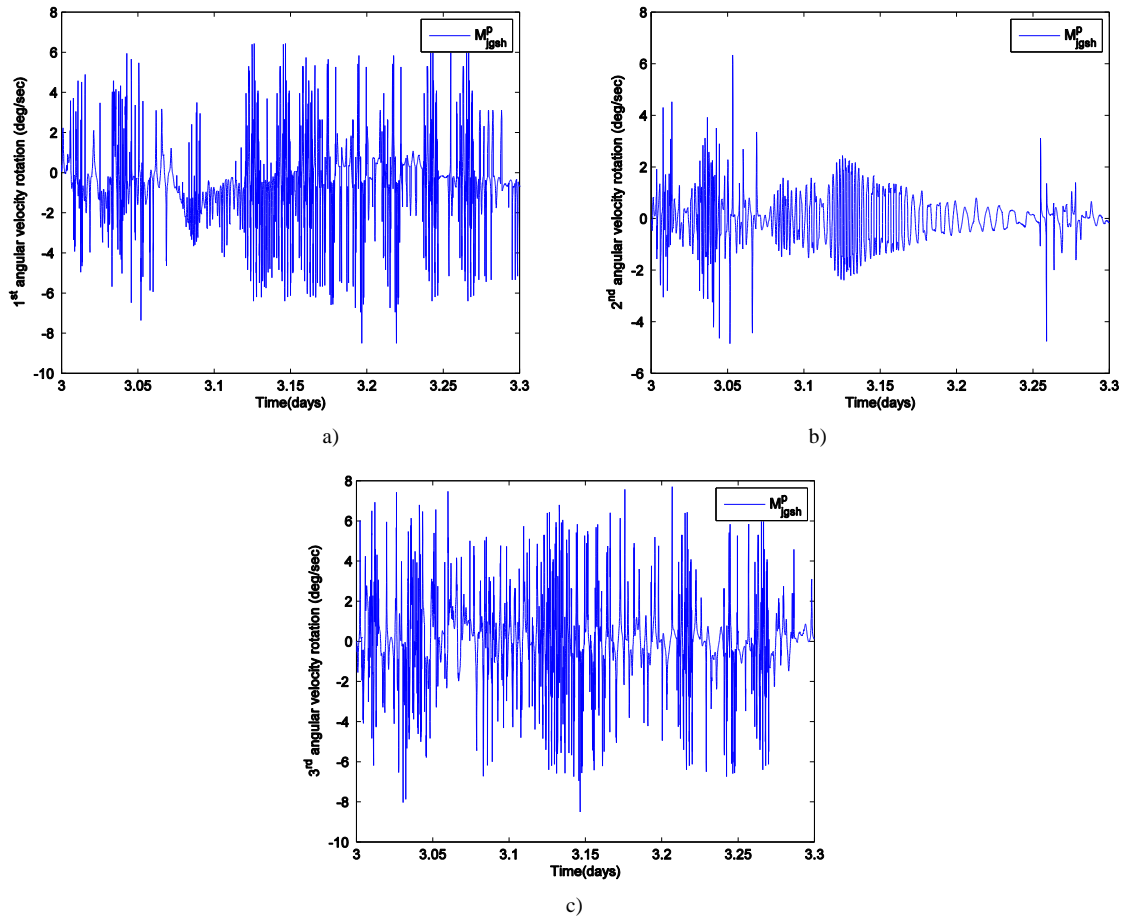

a)

b)

c)

Fig 29 Euler angle evolution of M^p_{jgsh} during 3.0-3.3 day under J_2, third body perturbations and the direct solar radiation pressure a) the 1st Euler rotation b) the 2nd Euler rotation c) the 3rd Euler rotation.
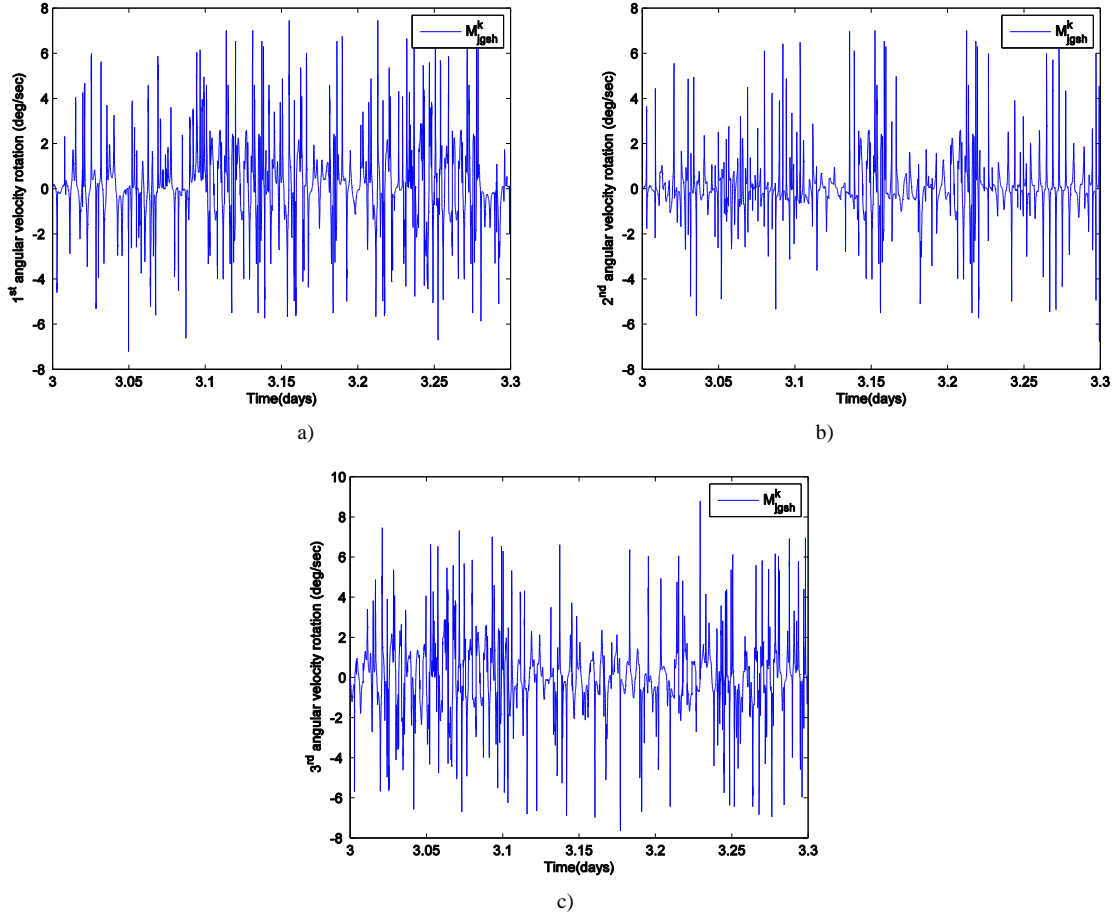
Fig 30 Euler angle evolution of M_{jgsh}^{k} during 3.0-3.3 day under J$_2$, third body perturbations and the direct solar radiation pressure a) the 1st Euler rotation b) the 2nd Euler rotation c) the 3rd Euler rotation.

5.3 Monte Carlo simulation

In a real case scenario the attitude and shape of the debris will not be known. Performing a Monte Carlo analysis can therefore shed some light on understanding the effects that different initial conditions have on the orbital propagation of the debris. A Monte Carlo simulation of the flexible model is therefore, performed to investigate the uncertainty of the orbital evolution over a period of 100 days under different initial attitude and deformation angle of the flexible model (M_{jgsh}^{p}) by comparing it with cannonball model (C_{jgs}^{p}) and flat rigid plate (R_{jgs}^{p} and RC_{jgs}^{p}). All objects will be in the same initial orbit shown in Table 2 and the same starting date. In the case of the rigid models, there are 3 cannonball objects with different AMR of 50, 70 and 111.11 m^2/kg and two flat rigid plates: R_{jgs}^{p} with AMR of 19.04 m^2/kg with averaged solar radiation pressure while for RC_{jgs}^{p} attitude and orbital dynamics (AMR 111.11 m^2/kg) are coupled.

The computational cost of a Monte Carlo simulation over 100 days for the flexible model is high, due to the coupling of shape deformation, attitude dynamics and orbital motion as well as the inclusion of self-shadowing effects when compared to the rigid model. The sampling technique is, therefore, important to select the suitable sampling sizes of initial rotational angles and deformation angle. From the study of Burhene and Matala by comparing different sampling methods (random

sampling, stratified sampling, Latin hypercube sampling and sampling based on Sobol sequence) (Matala, 2008, Burhenne et al., 2011), the Latin hypercube (LH) sampling shows the fastest convergence and produces reasonable results even for very small sample sizes. This technique is flexible in terms of data density and location and has good uniformity with respect to each dimension variable.

Fig 31 shows the mean value of the different sampling size of attitude angles and deformation angle of M_{jgsh}^p by varying the sample size. The sampling is performed according to a uniform distribution in the interval [0,1]. It can be seen that the distribution tends to converge at 300 samples, which RC_{jgs}^p will have the same intial orientation as M_{jgsh}^p. The mean and standard deviation (SD) of each variable are 0.5 and 0.2891 respectively. For the higher sample sizes at 500, 700 and 1,000 are very similar values (mean = 0.5, 0.5 and 0.5 and SD = 0.2890, 0.2890 and 0.2889 respectively). Due to the large number of sampling size and complicated flexible body dynamics the analysis requires a large computational effort. The simulations were, therefore, performed in 500 sample sizes and processed in parallel on a Linux-based computer cluster with 50 processor cores.
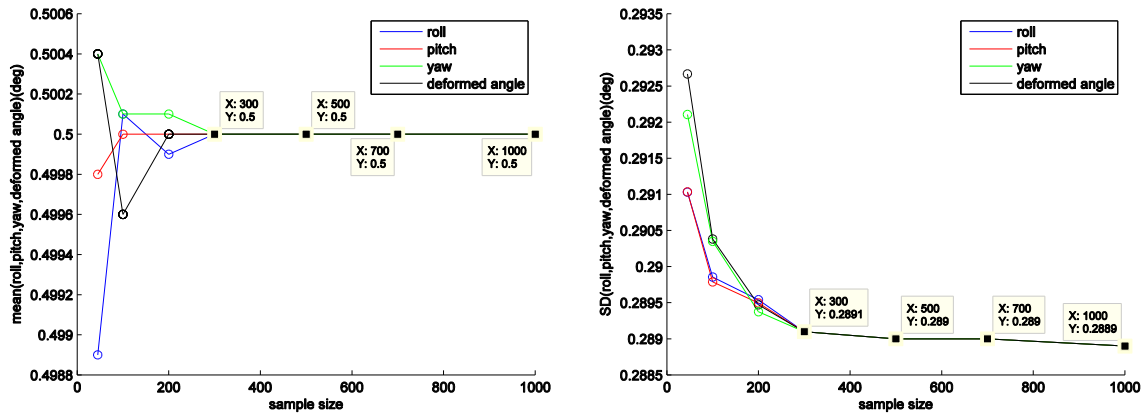

Fig 31 Comparing mean and standard deviation values of 4 variables (yaw, pitch, roll and deformed angle) in different sampling size by using Latin hypercube method in term of uniform distribution [0,1].

Fig 32 shows the final values of eccentricity, inclination and semi-major axis for C_{jgs}^p, R_{jgs}^p, RC_{jgs}^p and M_{jgsh}^p over 50 days. It can be noticed that C_{jgs}^p with AMR: 111.11 (triangular marker) and R_{jgs}^p (cross marker) reach the highest and lowest eccentricity respectively and for C_{jgs}^p with AMR: 70 m²/kg (diamond marker), the orbital evolutions of this object is close to the debris cloud of M_{jgsh}^p. The evolution of 500 samples for both M_{jgsh}^p and RA_{jgs}^p plotted in term of the histogram and fitted distribution in Fig 33and Fig 34 shows that eccentricity, inclination and semi-major axis of M_{jgsh}^p are in range of 0.31–0.34, 4.30–4.62 degrees and 41,611–42,629 km respectively and for RC_{jgs}^p the eccentricity range of 0.38 – 0.52, inclination range of 3.80–5.12 degrees and semi-major axis of 41,748-42,482 km and Standard deviation values of RC_{jgs}^p in orbital elements are higher than those of M_{jgsh}^p. The non-Gaussian distributions of orbital evolutions of both M_{jgsh}^p and RC_{jgs}^p are presented due to the nonlinear dynamics of both models.
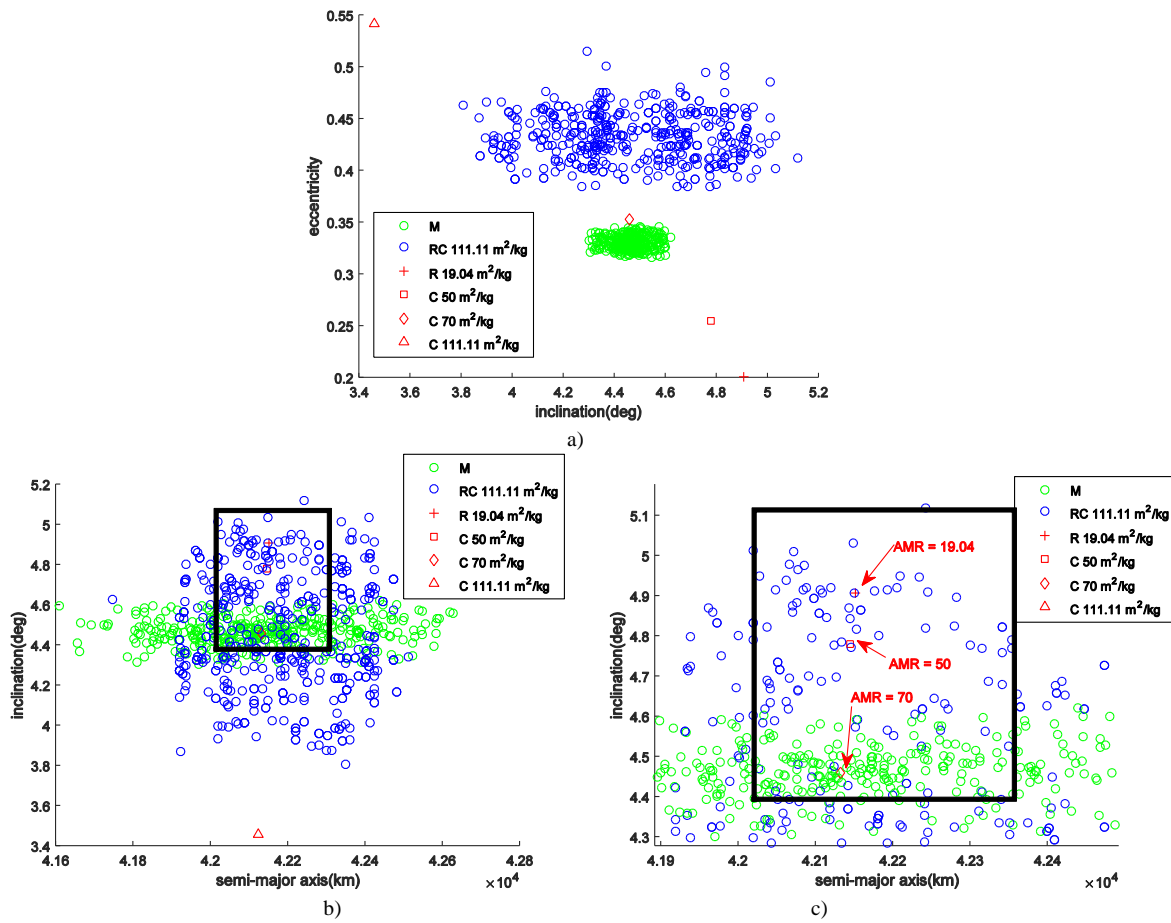
Fig 32 Comparison the orbital distribution of the Monte Carlo simulation of the flexible model with rigid flat plate and cannonball objects over 50 days a) inclination vs eccentricity b) semi-major axis vs eccentricity c) Magnify on the blue area of semi-major axis vs inclination.
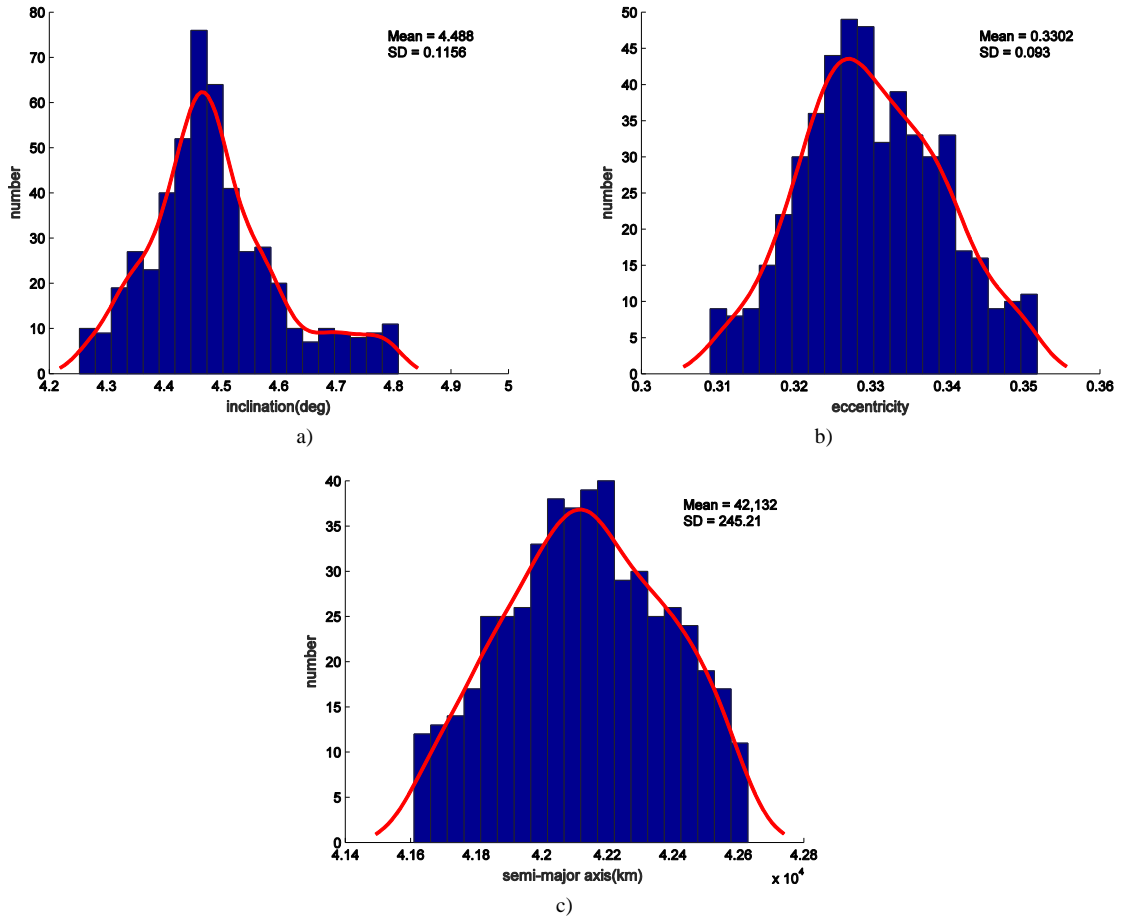
Fig 33 Histogram and fitted kernel distribution of orbital evolutions of M_{jgsh}^{p} over 50 days a) inclination (b) eccentricity (c) semi-major axis.
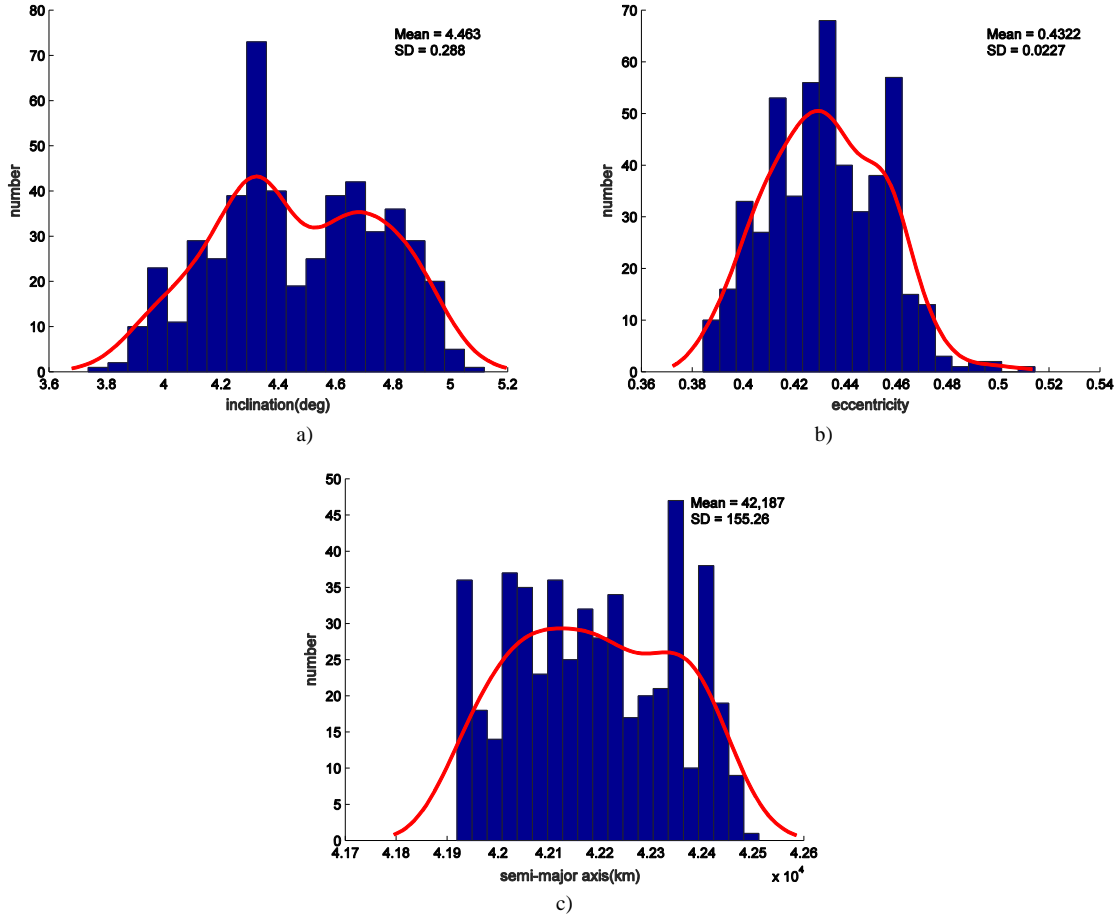
Fig 34 Histogram and fitted kernel distribution of orbital evolutions of RC_{jgs}^p over 50 days a) inclination (b) eccentricity (c) semi-major axis.

After evaluating the orbital dynamics over 100 days in Fig 35, all cannonball-type objects in Fig 35(b) move in the RC_{jgs}^p and M_{jgsh}^p clusters between semi-major axis range of 42,139-42,211 km with inclination range of 5.45- 6.98 degrees while the distributions of both M_{jgsh}^p and RC_{jgs}^p clouds in Fig 36 and Fig 37 displays larger areas when compared to the 50 days results M_{jgsh}^p: eccentricity range of 0.52–0.62, inclination range of 4.72–4.58 degrees and semi-major axis of 41,590-42,960 km and RC_{jgs}^p: eccentricity range of 0.62–0.83, inclination range of 5.26 – 8.77 degrees and semi-major axis of 41,690-42,677 km. As the results of the Monte Carlo simulations over 100 days, it is worthwhile noting that the different initial conditions of flexible model and flat rigid plate lead to unique evolution because both are subject to changes in the effective cross-sectional area, which results in large variations in the SRP force vector. However, the orbital prediction of a flat rigid plate coupled attitude and orbital motion is not appropriate for HAMR debris because the overestimation of AMR assumed as contant (no deformation) leads to less accuracy in the SRP radiation pressure effect when comparing with flexible model. In case of the cannonball model, the secular eccentricity is proportional to AMR value but the evolutions of both inclination and semi-major axis of cannonball model display narrower variations when compared to flexible model. These results support that the cannonball model and flat rigid plate despite using either an averaged area value or coupled attitude and orbital dynamics do not appear to provide a good approximation to the orbital dynamics of HAMR debris.

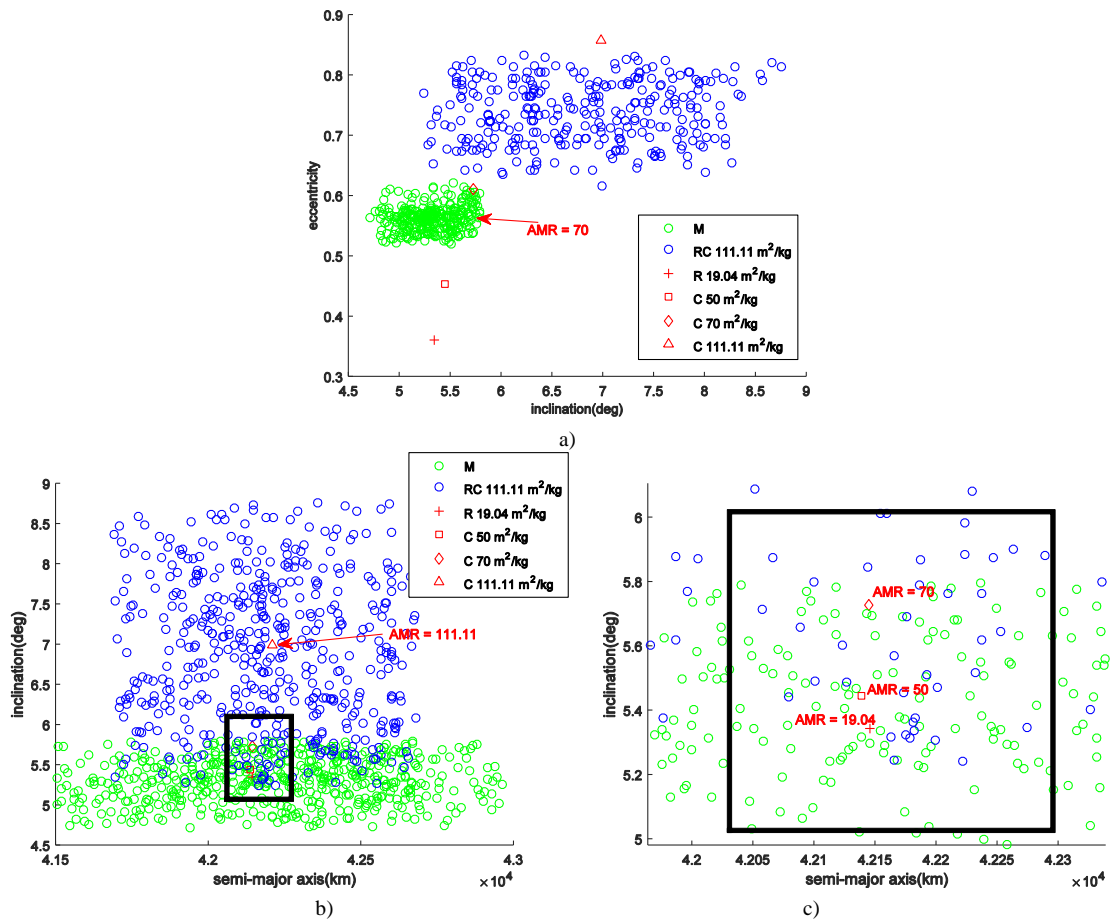Fig 35 Comparison the orbital distribution of the Monte Carlo simulation of the flexible model with flat rigid plate and cannonball objects over 100 days a) eccentricity vs inclination b) semi-major axis vs inclination c) Magnify on the blue area of semi-major axis vs inclination.
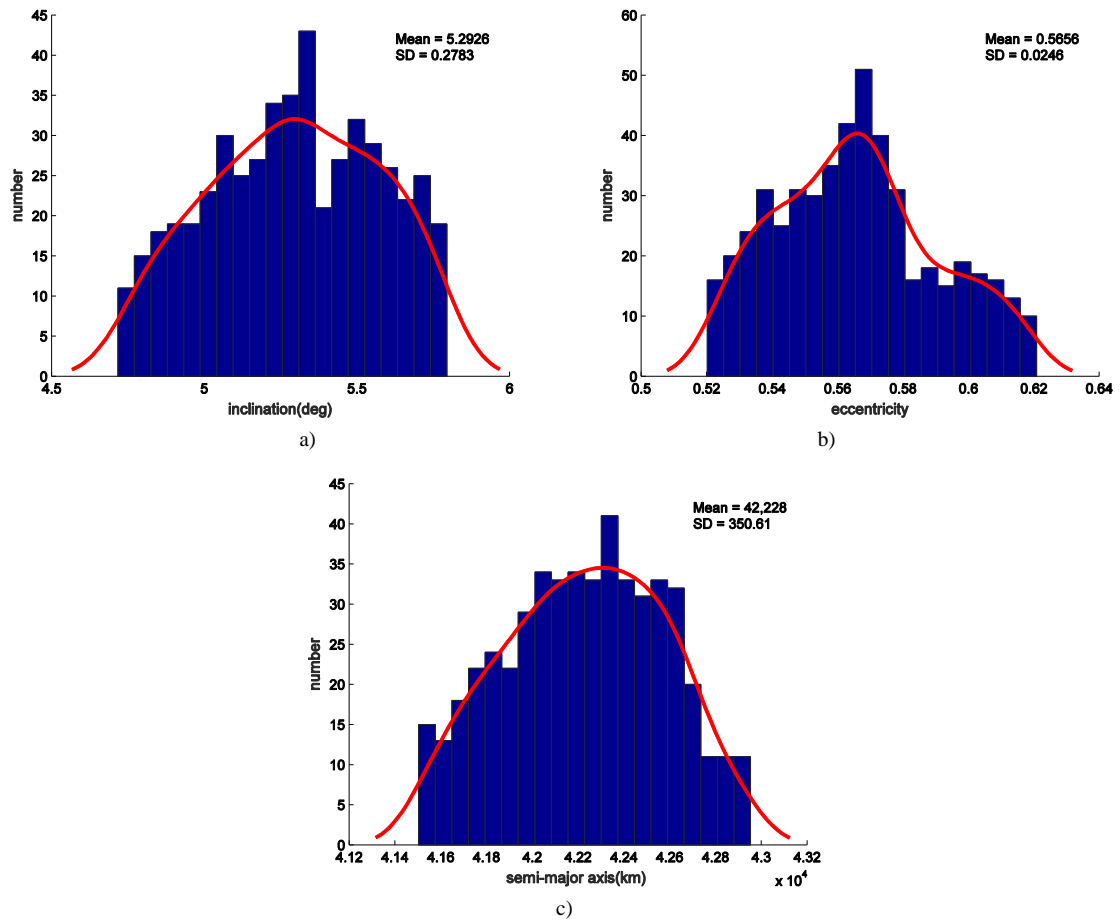
Fig 36 Histogram and fitted kernel distribution of orbital evolutions of M_{jgsh}^{p} over 100 days a) inclination (b) eccentricity (c) semi-major axis.
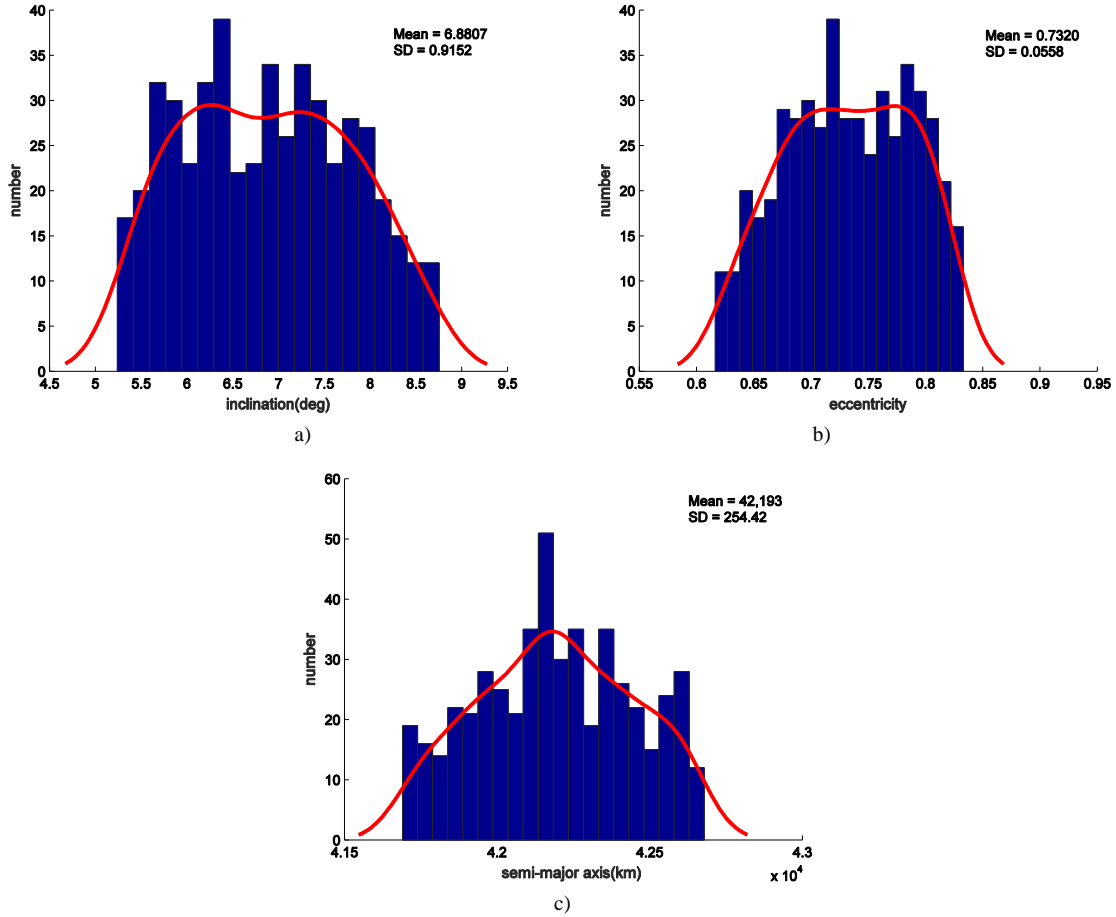
Fig 37 Histogram and fitted kernel distribution of orbital evolutions of RC_{jgs}^{p} over 100 days a) inclination (b) eccentricity (c) semi-major axis.

6. CONCLUSIONS

This paper purposes to introduce the new model for high area-to-mass ratio (HAMR) that can change a shape over time. The new model based on flexible dynamics that is able to couple deformation, attitude and orbit dynamics in near GEO region has been presented. The specific results of the effects of various perturbations on different orbital parameters and physical properties of the body are analysed. The cannonball shows the most rapid secular increase in eccentricity and the highest amplitudes in the daily change of the inclination. Compared to the orbital element evolutions of a flat rigid model, the flexible model displays larger changes in inclination and eccentricity. The fast rotation of the flexible model leads to inclination and eccentricity changes that are different from that of a flat rigid plate. Then, the self-shadowing effect provides different orbital and attitude dynamics, deformation and hence effective cross-section area when compared to a body without self-shadowing effects.

The J_2 and luni-solar perturbations can induce body rotation due to gravity torque. Larger area-to-mass ratios are also the reason for higher oscillations in both inclination and eccentricity as well as rapid irregular spin. In all simulations the results show that perturbations from solar radiation pressure also play a significant role in both the dynamical evolution and rapid complex rotation of the body.

According to the results of the Monte Carlo simulations, different initial conditions of in the attitude dynamics and shape orientation leads to substantially different orbital dynamics over a period of just 100 days. The results also appear to support the idea that rigid objects (cannonball and flat rigid plate) are not a good approximation to predict the short and long term orbital evolutions of HAMR debris. The computational cost of the flexible model consumes significantly higher than traditional models (cannonball and rigid flat plate coupled attitude and orbital motions) due to the nonlinear dynamics of the flexible model but it is reasonable to implement when comparing with FEM more degrees. The accuracy of the model can be improved by tightening the propagation tolerance (RelTol and AbsTol) but this significantly effects a computational time.

However, the flexible method makes a use of discrete rotational springs and dampers to account for the bending stiffness of the membrane from Eq. (7) and (8). The spring and damper constants were estimated through semi-empirical formulas, based on the data of the materials of the typical MLI membranes. These estimations however can be wrong because of the extremely thin nature of the membrane itself. Future work will therefore focus on the definition of an experimental setup, through the use of a vacuum chamber replicating the space environment to determine the characteristics of the material (damping ratio) and natural frequency of real multilayer insulation to allow the validation of the flexible model through experimental results.

The outcomes of this paper have a direct effect on the ability to predict the short and long term evolution of HAMR debris. It will provide a clearer understanding of MLI-type debris. This model is enable to the community to develop appropriate mitigation strategies and enhances the reliability and success probability of current and future space mission by minimising the possibility of debris impact. Other application areas can also benefit from this work. More accurate orbital propagation of space debris can enhance active debris removal concepts such as drag sail or robotic arm or allow the development of new concepts for space debris removal. Additionally flexible spacecraft appendages such as antennas and solar panels can benefit from the flexible model developed here as attitude slews often cause dynamic deformation in these structures. Finally, more accurate prediction of solar sail dynamics can be improved by extending the flexible model to the entire sail as well as future large space structures, which such as solar power satellites which will be highly flexible and have high area to mass ratio.

Acknowledgements

References

Blackburn, E. P., Sabroff, A. E., Bohling, R. F., Dobrotin, B., Fischell, R., Fleig, A. J., Kelly, J., Fosth, D., O'Neill, S., Spenny, C. H., Perkel, H., Roberson, R. E., Scott, E. D. & Tinling, B. 1969. Spacecraft gravitational torques. *NASA space vehicle design criteria (guidance and control)*.

Blinn, J. F. 1988. Jim blinn's corner: Me and my (fake) shadow. *IEEE Computer Graphics & Applications8.,* 82-86.

Bohling, R. F., Carroll, F. J., Clark, J. P., Debra, D. B., Dobrotin, B. M., Fischell, R. E., Fleig, A. J., Fosth, D., Gatlin, J. A., Perkel, H., Roberto, R. E., Sabroff, A. E., Scott, E. D., Spenny, C. H. & Tinling, B. E. 1969. Spacecraft radiation torques.

Burhenne, S., Jacob, D. & Henze, G. P. Sampling based on sobol/sequences for monte carlo techniques applied to building simulation. 12th Conference of International Building Performance Simulation Association, 2011 Sydney.

Dever, J. A., Groh, K. K. d., Townsend, J. A. & Wang, L. L. 1998. Mechnical properties degradation of TEFLON FEP returned from the hubble space telescope. *36th Aerospace Sciences Meeting&Exhibit.*

Eisemann, E., Schwarz, M., Assarsson, U. & Wimmer, M. (eds.) 2012. *Real-time shadows*: CRC press,Taylor & Francis Group.

Früh, C., Ferguson, D., Lin, C. & Jah, M. Passive Electrostatic Charging of Near-Geosynchronous Space Debris HAMR Ojects and its Effects on the Coupled Object Dynamics. Proc. AAS Space Flight Mechanics Meeting, 2014 Santa Fe, NM.

Früh, C. & Jah, M. 2014. Coupled orbit-attitude motion of high area-to-mass ratio (HAMR) objects including efficient self-shadowing. *Acta Astronautica,* 95**,** 227-241.

Früh, C., Kelecy, T. M. & Jah, M. K. 2013. Coupled Orbit-Attitude Dynamics of High Area-to-Mass Ratio (HAMR) Objects: Influence of Solar Radiation Pressure, Shadow Paths and the Visibility in Light Curves. *Celestial Mechanics and Dynamical Astronomy (CELE).*

Früh, C. & Schildknecht, T. 2011. Variation of Area-to-Mass-Ratio of HAMR Space Debris objects. *Monthly Notices of the Royal Astronomical Society,* 419**,** 3521-3528.

Früh, C. & Schildknecht, T. 2012. Attitude Motion of Space Debris Objects Under Influence of Solar Radiation Pressure And Gravitiy. *63rd international Astronautical congress.* Naples, Italy.

Goodfellow. 2014. *Properties of products* [Online]. Huntingdon England. Available: http://www.goodfellow.com/.

Hubaux, C. & Lemaitre, A. 2013. The impact of Earth's shadow on the long-term evolution of space debris. *Celestial Mechanics and Dynamical Astonomy,* 116**,** 79-95.

Kubo-oka, T. & Sengoku, A. 1999. Solar radiation pressure model for the relay satellite of SELENE. *Earth Planets Space,* 51**,** 979-986.

Liou, J.-C. & Weaver, J. K. Orbital Dynamics of High Area-To Ratio Debris and Their Distribution in the Geosynchronous Region. Proceedings of the 4th European Conference on Space Debris, 2005 Darmstadt, Germany. 285.

Luthcke, S. B., Marshall, J. A., Rowton, S. C., Rachlin, K. E., Cox, C. M. & Williamson, R. G. 1997. Enchance Radiative Force Modeling of The Tracking and Data Relay Satellites. *American Astronomical Society Jornal,* 45**,** 349-370.

Matala, A. 2008. *Sample Size Requierement for Monte Carlo - simulation using Latin Hypercube Sampling,* Helsinki Universtiy of Technology.

McMahon, J. W. & Scheeres, D. 2015. Improving Space Object Catalog Maintenance Through Advances in Solar Radiation Pressure Modeling. *Journal of Guidance, Control and Dynamics,* 38**,** 1366-1381.

McMahon, J. W. & Scheeres, D. J. High-fidelity solar radiation pressure effects for high area-to-mass ratio debris with changing shapes. Proceeding AAS/AIAA Astrodynamics Specialist Conference, 2013 Hilton Head Island, South Carolina Paper AAS 13-763.

Mozurkewich, D. 2011. Toward Realistic Dynamics of Rotating Orbital Debris and Implications for Lightcurve Interpretation. *Advanced Maui Optical and Space Surveillance Technologies Conference.* Maui, Hawaii.

Murakami, J., Hanada, T., Liou, J.-C. & Stansbery, E. 2008. *Micro-satellite impact tests to investigate multi-layer insulation fragments.* PhD, Kyushu University.

Pavlis, D. D., Luo, S., Dahiroc, P., McCarthy, J. J. & Luthke, S. B. 1998. *GEODYN-II,* Grrenbelt, Maryland.

Rosengren, A. J. & Scheeres, D. J. 2013. Long-term dynamics of high area-to-mass ratio objects in high-Earth orbit. *Addvances in Space Research,* 52**,** 1545-1560.

Schaub, H. & Junkins, J. L. 2003. *Analytical mechanics of space systems*, American Institute of Aeronautics and Astronautics.

Schildknecht, T., Musci, R. & Flohrer, T. 2008a. Properties of the high area-to-mass ratio space debris population at high altitudes. *Advances Space in Research,* 41**,** 1039-1045.

Schildknecht, T., Musci, R., Früh, C. & Ploner, M. Color photometry and light curve observations of space debris in GEO. Proceedings of Advanced Maui Optical and Space Surveillance Technologies Conference, 17-19 September 2008b Maui Hawaii.

Schildknecht, T., Musci, R., Ploner, M., G., B., Flury, W., Kuusela, J., De Leon Cruz, J. & De Fatima Dominguez Palmero, L. 2004. Optical observation of space debris in GEO and in highly-eccentric orbits. *Advance Space in Research,* 34**,** 901-911.

Seeber, G. 1993. Satellite Geodesy. *Walter de Gruyter.*

Sen, L., Shen-wei, L., Zhaoxia, M. & Jie, H. 2012. A model to describe the size distribution of satellite breakup debris. *63rd International Astronautical Congress.* Naples, Italy.

Sheldahl. 2012. *The red book* [Online]. Available: http://www.sheldahl.com/documents/RedBook%20revised%2020-AUG%20%202012.pdf.

Valk, S. & Lemaître, A. 2008. Semi-analytical investigations of high area-to-mass ratio geosynchronous space debris including Earth's shadowing effects. *Advances in Space Research,* 42.

Valk, S., Lemaitre, A. & Anselmo, L. 2008a. Analytical and semi-analytical investigations of geosynchronous space debris with high area-to-mass ratio. *Advances in Space Research,* 41.

Valk, S., Lemaître, A. & Deleflie, F. 2008b. Semi-analytical theory of mean orbital motion for geosynchronous space debris under gravitational influence. *Advances in Space Research,* 43**,** 1070-1082.

Vallado, D. A. 2007. *Fundamentals of Astrodynamics and Applications,* New York, Microcosm Press.

Walker, M. J. H., Owen, J. & Ireland, B. 1985. A set of modified equinoctial orbit elements. *Celestial Mechanics* 36**,** 409-419.

Weisstein, E. W. 2016. *Sphere point picking* [Online]. Available: http://mathworld.wolfram.com/SpherePointPicking.html.

Williams, L. 1978. Casting Curved Shadows On Curved Surfaces. *SIGGRAPH Comput. Graph,* 12**,** 270-274.